ARMY RESEARCH LABORATORY ARL

New Laboratory-Scale Method for the Determination of Explosive Performance From Laser-Induced Shock Waves

by Jennifer L. Gottfried

ARL-TR-6844 March 2014

NOTICES

Disclaimers

The findings in this report are not to be construed as an official Department of the Army position unless so designated by other authorized documents.

Citation of manufacturer's or trade names does not constitute an official endorsement or approval of the use thereof.

Destroy this report when it is no longer needed. Do not return it to the originator.

Army Research Laboratory
Aberdeen Proving Ground, MD 21005-5069

ARL-TR-6844 **March 2014**

New Laboratory-Scale Method for the Determination of Explosive Performance From Laser-Induced Shock Waves

Jennifer L. Gottfried
Weapons and Materials Research Directorate, ARL

REPORT DOCUMENTATION PAGE	Form Approved OMB No. 0704-0188

1. REPORT DATE *(DD-MM-YYYY)*	2. REPORT TYPE	3. DATES COVERED (From - To)
March 2014	Final	1 October 2012–30 September 2013

4. TITLE AND SUBTITLE
New Laboratory-Scale Method for the Determination of Explosive Performance From Laser-Induced Shock Waves

5a. CONTRACT NUMBER

5b. GRANT NUMBER

5c. PROGRAM ELEMENT NUMBER

6. AUTHOR(S)
Jennifer L. Gottfried

5d. PROJECT NUMBER
622618H80

5e. TASK NUMBER

5f. WORK UNIT NUMBER

7. PERFORMING ORGANIZATION NAME(S) AND ADDRESS(ES)
U.S. Army Research Laboratory
ATTN: RDRL-WML-B
Aberdeen Proving Ground, MD 21005-5069

8. PERFORMING ORGANIZATION REPORT NUMBER
ARL-TR-6844

9. SPONSORING/MONITORING AGENCY NAME(S) AND ADDRESS(ES)

10. SPONSOR/MONITOR'S ACRONYM(S)

11. SPONSOR/MONITOR'S REPORT NUMBER(S)

12. DISTRIBUTION/AVAILABILITY STATEMENT
Approved for public release; distribution is unlimited.

13. SUPPLEMENTARY NOTES

14. ABSTRACT
A new laboratory-scale method for predicting explosive performance (e.g., detonation velocity and pressure) based on milligram quantities of material is currently being developed. This technique is based on schlieren imaging of the shock wave generated in air by the formation of a laser-induced plasma on the surface of an energetic material residue. Various conventional energetic materials, including RDX, TNT, HMX, PETN, HNS, TATB, CL-20, composition-B, composition-A5, and Pentolite, have been tested. Preliminary results show a linear correlation between the laser-induced shock velocity and the measured performance from full-scale detonation testing. This method is a potential screening tool for the development of new energetic materials and formulations prior to larger-scale detonative testing.

15. SUBJECT TERMS
energetic materials, laboratory-scale, laser ablation, laser-induced shock waves, plasma chemistry

16. SECURITY CLASSIFICATION OF:			17. LIMITATION OF ABSTRACT	18. NUMBER OF PAGES	19a. NAME OF RESPONSIBLE PERSON
a. REPORT	b. ABSTRACT	c. THIS PAGE			Jennifer L. Gottfried
Unclassified	Unclassified	Unclassified	UU	64	19b. TELEPHONE NUMBER (*Include area code*) (410) 278-7573

Standard Form 298 (Rev. 8/98)
Prescribed by ANSI Std. Z39.18

Contents

List of Figures

List of Tables

1. Introduction

The interaction of focused laser pulses with different materials has been an active area of study since the invention of the first laser in 1962 (*1*). Laser ablation has been used for spectroscopic material characterization, sample introduction for chemical analysis techniques, laser machining, laser cleaning, thin film deposition, nanoparticle production, medical applications, etc. The processes involved in the excitation of a material using a high-energy focused laser pulse, including material ablation, expansion into a background gas, plasma ignition, chemical reactions (during and after plasma formation), shock waves, and particle formation, are extremely complicated and cannot be described by a single model. The behavior of the excited material is highly dependent on the material properties (e.g., density, thermal conductivity, absorption coefficient, melting point, and ionization potential), the laser properties (e.g., pulse wavelength, duration, and energy), and the background gas (e.g., composition and pressure). Figure 1 lists the processes involved in the laser ablation of a target material.

During the initial laser-solid interaction, target heating, melting, and vaporization occur. These thermal processes are described by models based on the thermal heat conduction equation (*2*). As the material is removed by the pulsed laser, pressure is built up by the volumetric gain of the ablated particles due to the change in their specific volume during the transition from a condensed state to the vapor state. At sufficient laser pulse energies (irradiances greater than 10^{10} W/cm^2), explosive boiling of the target material beneath the surface layer, called phase explosion, leads to mass removal via the ejection of large particles from the sample surface; the ejection of particles can continue for hundreds of milliseconds (*3–7*). Expansion of the evaporated material into the background gas is extremely rapid and can be described by the Euler equations of hydrodynamics (*2*, *8*). Generation of a laser-induced plasma begins by absorption of the laser energy through inverse bremsstrahlung processes (absorption of a photon by a free electron), leading to a rapid temperature rise. The hot vapor layer above the sample surface is completely ionized at a pressure substantially above the ambient pressure. Atoms, molecules, and ions undergo collisions in a region above the sample surface called the Knudsen layer (*9*). Light emission collected from the plasma can thus produce information about the elemental content of the sample in a technique called laser-induced breakdown spectroscopy, or LIBS (*10*). The LIBS spectra of energetic materials have been investigated for standoff detection applications (*11–13*). Typical plasma temperatures reach tens of thousands of kelvin and are substantially higher for energetic samples than for nonenergetic materials.

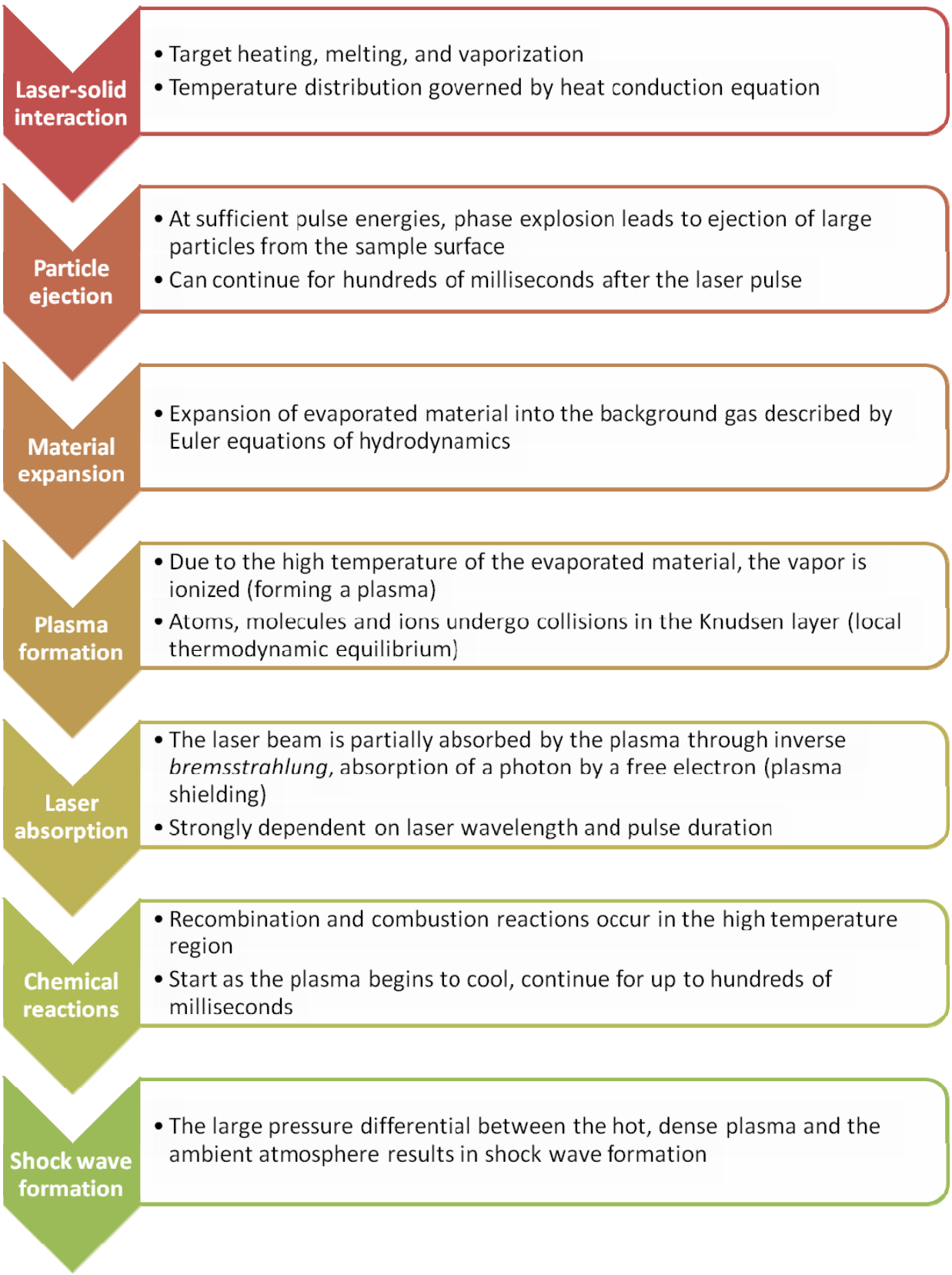

Figure 1. Interdependent processes involved in the laser ablation of a target material.

For longer-pulse lasers (greater than 100 ps), the laser beam is partially absorbed by the plasma through inverse bremsstrahlung in a process called plasma shielding (*14*). This process can rapidly increase the plasma size and temperature and is strongly dependent on laser wavelength and pulse duration. Near-infrared laser wavelengths (e.g., 1064 nm) are particularly efficient at heating the plasma compared with visible and ultraviolet wavelengths. Once the laser heating has ended, the plasma begins cooling rapidly for the first 100 ns; after 100 ns, plasma cooling is slowed as energy is regained through recombination and combustion reactions (*15, 16*). Thermal energy from the material in the plasma is converted to kinetic energy, resulting in high expansion velocities. The expansion of the high-pressure vapor acts as a piston driving into the surrounding atmosphere, compressing the ambient gas at its front into a thin shell. For laser ablation, the force of this piston depends on the volume of gas produced, which is related to both the ablated mass and to the temperature reached in the plasma plume. Energy is transferred to the surrounding air through a combination of thermal conduction, radiative transfer, and heating by the resulting shock wave. At high laser irradiances, shock heating dominates (*17*).

When the plasma dynamics are determined by absorption of the laser radiation within the plasma, the shock wave is similar to a detonation phenomenon and is called a blast wave (*18–20*). Both the laser-induced plasma generated from a thin film of material applied to a glass substrate and the shock structure of the resulting blast wave are shown in figure 2. The arrows indicate the direction of propagation for the plasma and various fronts. The presence of the contact fronts, ionization front, and shock front has been confirmed through shadowgraph imaging (e.g., Callies et al. [*21*]). The propagation of the blast wave is determined by the amount of energy released into the plasma state. The Sedov-Taylor theory can be used to describe the blast waves (*19*, *21*, *22*). For spherical propagation, the relationship between the distance travelled by the blast wave R and the energy converted into the plasma state ΔE is given by

$$R = \lambda \left(\frac{\Delta E}{\rho_0} \right)^{1/5} t^{2/5} \tag{1}$$

where λ (with an approximate value of 1) is a dimensionless quantity depending on the gas-dynamical state of the air, ρ_0 is the mass density of the undisturbed air, and t is the time of propagation (assuming the laser pulse duration is less than t and the laser spot diameter is less than R). Equation 1 is only valid when the mass of energy source is negligible compared with the mass of the surrounding air that is swept up by the expanding shock (i.e., not valid at very early times) and when the pressure driving the shock's front is much larger than the pressure ahead of it ($R \ll (\Delta E/\rho_0)^{1/3}$), a condition not met after a certain distance. The expansion of the shock wave produced with a nanosecond laser was found to be spherical and proportional to $t^{2/5}$ from about 3–100 ns (*23*).

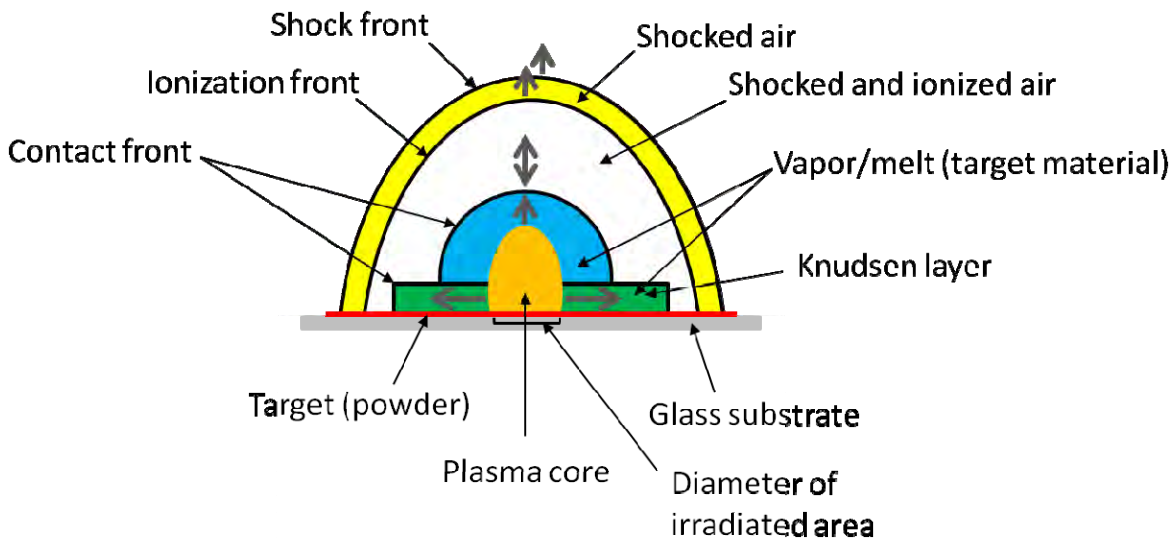

Figure 2. Laser-induced plasma and shock structure.

At high laser irradiances (typically higher than 10^7 W/cm^2), a shock front analogous to a detonation can be ignited from nearly any material (*24*). The interaction of the laser beam with the plasma results in compression of the vaporized gas by the absorption of the laser energy, contributing to the heating and ionization of the ablated material. The velocity in this region is supersonic with respect to the ambient gas, and a shock wave known as a laser-supported detonation wave (LSDW) is produced (*3*, *24–28*). The name LSDW originated from its similarity to a chemical explosion, which propagates by shock compression of a combustible mixture. In this regime, laser energy is absorbed by the plasma in front of the shock wave, and the shock wave is efficiently enhanced; at irradiances lower than 10^6 W/cm^2, laser-supported combustion occurs and the laser energy is absorbed in the plasma behind the shock wave with no contribution to the thrust from the blast wave expansion (*28*).

The properties of the LSDW are dependent on the gas species and the pressure through which the wave propagates. The LSDW creates a high-temperature and pressure region that enables atomic and molecular reactions which could lead to a chemical detonation. For example, Kim et al. (*29*) compared the initiation of chemical reactions between ablated aluminum and oxygen from the air with a high-power laser pulse to the classical detonation of exploding aluminum dust in air, while Gottfried (*15*) investigated the chemical reactions between laser-ablated metal particles and the explosive cyclotrimethylenetrinitramine (RDX). Typical shock wave velocities near the laser-material interaction region are tens of kilometers per second, corresponding to pressures of tens or hundreds of gigapascals (*3*, *8*). Unlike the spherical blast wave that propagates normal to the sample surface, the LSDW is conical in shape and propagates along the direction of the laser beam (figure 3). The LSDW lasts only as long as the propagation conditions are satisfied during the laser pulse, i.e., as the laser beam diverges with increasing distance from the target, the wave degenerates into a combustion wave with a much smaller absorption coefficient.

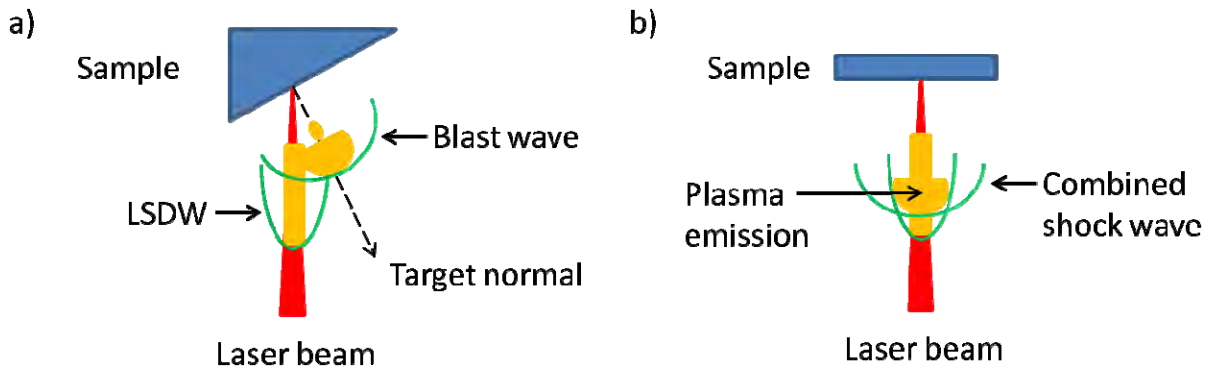

Figure 3. Comparison of the LSDW and blast waves, which are distinct when the laser interrogates the sample off-angle (a) and combined when the propagation of the laser is perpendicular to the sample (b).

As the shock wave expands into the ambient atmosphere, resistance from collisions of the shocked air with the background gas decelerates the shock wave; an internal shock wave generated by the deceleration of the contact front by the background gas is propagated back toward the target surface and is reflected back and forth between the sample surface and the external shock front until the external shock has dissipated into a sound wave. At later times the distance of the external shock wave from the target *R* can be described by a drag model (*30*), which is given by

$$R = R_0 \left[1 - e^{-\beta t}\right] \tag{2}$$

where R_0 is the stopping distance of the shock wave and β is the slowing coefficient (resulting from resistance caused by collisions with the background gas). Eventually the shock is dissipated as a result of this drag/resistive force. Previous studies on the expansion dynamics of the laser-induced plasma have shown that the plume expansion follows the blast wave model (equation 1) up to 300 ns (*31*), and the drag model is a good approximation of the plume front velocity $v_0 = R_0\beta$ from 500 to 2000 ns (*9*). At times greater than 4 μs, the drag model was found to predict distances slightly shorter than those observed experimentally (*32*). Similar results have been obtained for the shock wave expansion, although most use either equations 1 or 2, depending on the experimental conditions (*21*, *23*, *30*, *33–45*).

The Rankine-Hugoniot jump equations describe the conservation of mass, momentum, and energy across a shock front (*46*). The simplified jump equations (when the unshocked material is at rest and at low ambient pressure) are given by

$$\frac{\rho_1}{\rho_0} = \frac{U}{U - u_1} \tag{3}$$

$$P = \rho_0 u_1 U \tag{4}$$

and

$$e_1 - e_0 = \frac{1}{2} P \left(\frac{1}{\rho_0} - \frac{1}{\rho_1} \right) \tag{5}$$

where P is the shock pressure, U is the shock velocity, u is the particle velocity, ρ is the density, and e is the internal energy (subscripts 0 and 1 refer to the unshocked and shocked material, respectively). The shock velocity U is linearly related to the particle velocity u according to an empirical relationship called the velocity Hugoniot equation,

$$U = C_0 + su \tag{6}$$

where C_0 is the bulk sound speed (no physical meaning) and s is the velocity coefficient for the material. The properties of shocked air have been previously determined (*47*, *48*), at 1 atm, C_0 = 0.2409 km/s and s = 1.0602 for air (*48*). By combining equations 4 and 6, we can then calculate the peak shock pressure in air (Pa) using only the measured air shock velocity (in meters per second):

$$P = \rho_0 \left(\frac{U - c_0}{s} \right) U = 1.2041 \left(\frac{U - 240.9}{1.0602} \right) U \tag{7}$$

Following the laser-induced plasma and subsequent shock wave formation, ejected material above the sample surface can begin to deflagrate several milliseconds after the initial laser shot (especially for energetic materials); this deflagration can last for hundreds of milliseconds and provide useful spectroscopic information about the combustion reactions of the material in air (*49–52*). The focus of the current study, however, is how the velocity of the shock wave is affected by the target material properties. Most previous studies on laser-induced shock waves used silicon or metal targets and focused on how the shock structure was influenced by the parameters such as the background gas or the laser parameters (e.g., *8*, *19*, *21*, *23*, *37*, *39–41*, *43*, *44*, *53–56*). However, a few studies found that a laser-ablated energetic polymer (glyzidyl azide polymer [GAP]) produced a faster shock wave than nonenergetic polymers (*57–60*). The increased shock wave velocity was attributed to the higher decomposition enthalpy of GAP; the pulsed laser initiated a self-sustaining exothermic reaction resulting in rapid formation of gaseous products. More recently, Roy et al. (*45*) measured spatially and temporally resolved temperatures behind an expanding laser-induced shock wave to demonstrate differences in energy release between reacting aluminum nanoparticle formulations.

Here, the shock wave velocity in air at different positions above the sample surface generated from a large variety of inert and energetic materials was measured to determine the effect of chemical reactions on the laser-induced shock wave. The ultimate goal of this research is to develop a laboratory-scale method for estimating detonation performance using milligram quantities of energetic materials. Kleine et al. (*61*) have verified that blast wave scaling laws, which have been confirmed for detonation tests ranging from 1 to 10^9 g, also apply to charges in the milligram range. Large-scale testing (hundreds to millions of grams of explosive) is expensive and time consuming; in addition, diagnostics are difficult because of the inherently

destructive nature of the tests and the opaqueness of the early fireball. In many cases, scaling up production of new types of energetic materials for large-scale testing is prohibitively expensive without some a priori assurance of performance gains over conventional explosives. The ideal small-scale test, on the other hand, would not require any scale-up or formulation of potential new energetic materials and could safely be performed in a laboratory environment with minimal cost per test.

2. Experimental

2.1 Sample Preparation

Energetic material samples were obtained from colleagues at the U.S. Army Research Laboratory (ARL); materials investigated included black powder, smokeless gun powder, 1,3-dinitrobenzene (m-DNB), 1,4-dinitrobenezene (p-DNB), trinitrotoluene (TNT), RDX (class 1 and class 5), hexanitrostilbene (HNS), triaminotrinitrobenzene (TATB), pentaerythritol trinitrate (PETN), cyclotetramethylene tetranitramine (HMX), hexanitrohexaazaisowurtzitane (CL-20), Composition-A5 (RDX coated with 1.5% stearic acid), Composition-B (60% RDX, 40% TNT), and Pentolite (50% PETN, 50% TNT). Inert materials, including ammonium nitrate (AN)(NH_4NO_3), Epsom salt ($MgSO_4 \cdot 7H_2O$), L-glutamine ($C_5H_{10}N_2O_3$), melamine ($C_3H_6N_6$), sugar (sucrose, $C_{12}H_{22}O_{11}$), graphite nanoparticles (GNP; 3–4 nm), nanographite (NG; 1–4 μm wide, 50 nm thick), diamond grit (25–35 μm), and graphite lubricant (micron-sized particles), were obtained from various commercial sources. All samples (table 1) were prepared on the same substrate: double-sided tape affixed to a glass micro slide (25 × 75 mm). Approximately 10–20 mg of each material was applied to the tape surface and distributed across the surface with a spatula. Excess material was removed by gently tapping the slide. Since the shock wave from each laser shot removed material from a diameter approximately 500% larger than the diameter of the focused laser, subsequent laser shots were spaced to avoid disturbed areas of the sample surface. A total of 5–8 laser shots were obtained from each sample slide.

2.2 Laser Ablation

The laser pulse from an Nd:YAG laser (Quantel Brilliant b) was focused on the sample surface with a 10-cm lens (table 2). In order to prevent breakdown of the air above the target, the plane of the target surface was placed 1.5 mm above the focal point of the lens (i.e., 1.5 mm closer to the lens). The estimated diameter of the focused laser beam based on the average crater size on several metal targets was 0.8 mm. The highest laser pulse energy attainable with this laser was used to ensure breakdown of any target material and to ensure formation of an LSDW. Because the energetic materials were applied in a thin layer and shocked with a nanosecond-pulsed laser that is not sufficient to initiate the secondary energetic materials, no detonation wave was generated through the bulk energetic material. A strong exhaust inlet was positioned next to the

sample stage to remove vapors and particulate matter. The influence of the exhaust on the ablated material was not observed until several milliseconds after the initial laser pulse, when the heated air, unreacted particles, and deflagrating particles (for energetic materials) were pulled toward the exhaust (to the left of the camera view).

Table 1. Energetic and nonenergetic samples investigated.

Energetic materials	Non-energetic materials
Black powder	Blank (double-sided tape on glass slide)
Smokeless gun powder	Graphite lubricant (micron-size)
1,3-dinitrobenzene	Diamond (25-35 μm)
1,4-dinitrobenzene	Nanographite (1-4 μm wide, 50 nm thick)
HNS	Graphite nanoparticles (3-4 nm)
TNT	Sugar
RDX (Class 1 and Class 5)	Melamine
HMX	L-glutamine
PETN	Epsom salt
TATB	Ammonium nitrate
CL-20	
Composition-A5	
Composition-B	
Pentolite	

Table 2. Parameters for the Nd:YAG ablation laser.

Laser parameter	Value
Pulse wavelength λ	1064 nm
Pulse duration t_p	6 ns
Maximum pulse energy E_p	900 mJ
Spot area A	5.0×10^{-3} cm^2
Fluence ε	180 J cm^{-2}
Peak power density (irradiance) I	3.0×10^{10} W cm^{-2}

2.3 Schlieren Imaging

The schlieren imaging technique (*62*) was used to visualize the laser-induced shock wave in air. Figure 4 shows a simplified schematic of the experimental setup. An arc lamp (Newport Oriel model 66476) with a 200-W Hg-Xe ozone-free lamp (model 6290) served as the illumination source, which was focused onto the first mirror with an aspheric condenser lens. The light was collimated between the two schlieren mirrors (10.8-cm diameter, 114-cm focal length), which were spaced 211 cm apart. The sample was placed on a vertical stage in the test section between the two mirrors, and the ablation laser was focused on the sample surface from above. Changes in the refractive index of the air caused by the formation of the laser-induced plasma bent the light rays, so that when the light was focused after the second mirror, a knife edge placed at the focal spot could be used to cut out approximately half the light rays; the schlieren images thus correspond to the first spatial derivative of the index of refraction. A high-speed color camera (Photron SA5) was used to record the light and dark striations in the images representing differences in the refractive index of air in the test region. A zoom lens (Nikon Nikkor 24–85 mm f/2.8-4D IF) on the camera was focused 33 cm in front of the focus of the ablation laser. This focal position was optimized to provide the greatest contrast for visualization of the shock wave. The following camera settings were used for imaging the shock waves: 84,000 frames per second (fps), 1.0-µs shutter, 64- × 648-pixel image size.

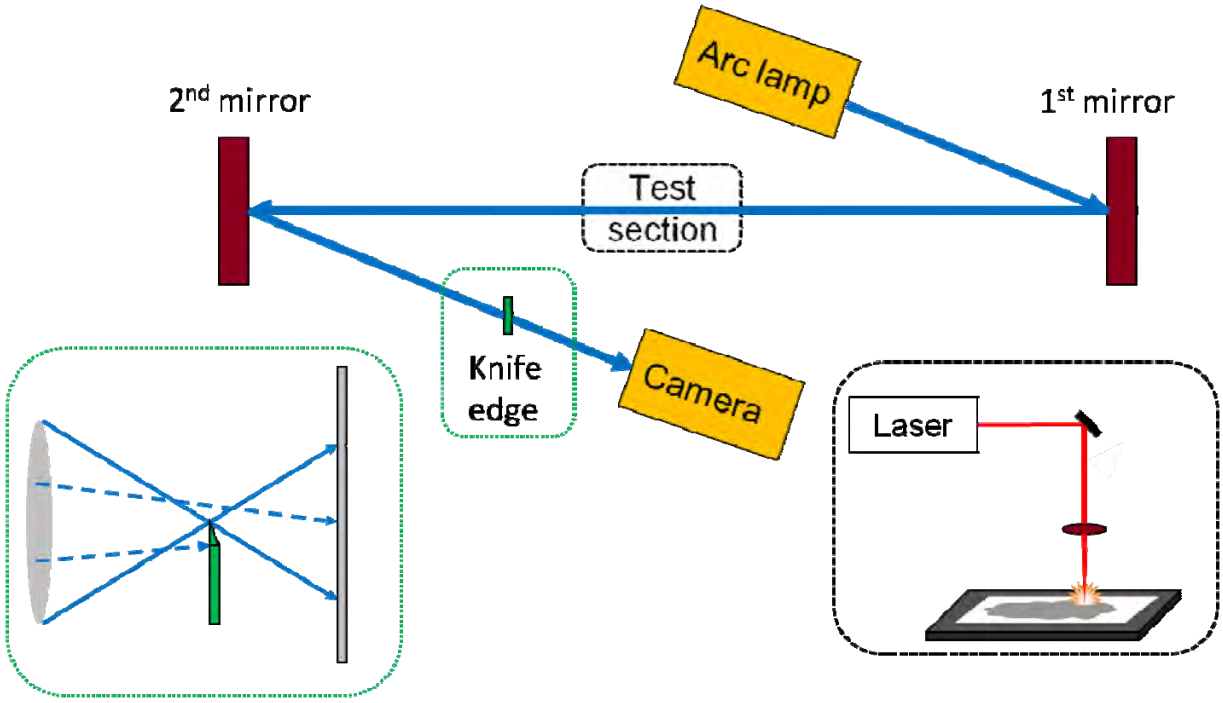

Figure 4. Experimental setup for schlieren imaging of the laser-induced shock wave.

3. Laser-Induced Shock Waves

3.1 Hemispherical Shock Wave Propagation

Figure 5 shows snapshots from the videos (12,000 fps at full camera resolution, 9.8-μs shutter) of the laser ablation of a nonenergetic material (L-glutamine) and an energetic material (RDX). The first frame after the laser pulse (0 μs) shows the laser-induced plasma, which is typically more luminescent for nonenergetic materials. Because of the decrease in brightness, the laser-induced shock wave is visible in the first frame of the RDX video. The second frame (83 μs) shows the roughly hemispherical propagation of the shock wave (which is faster for the RDX). The vertical height of the shock wave was approximately 50% of the horizontal diameter at the target for both samples. The high-resolution video also shows the ejection of material from the target surface, resulting from the impact of the internal shock wave. By 500 μs, the light emission was gone for both materials, and the heat-affected zone in the background air caused by the plasma formation was clearly visible for both samples; the RDX produces a significantly larger zone. At later times (greater than 1 ms), the pull of the exhaust on the heated air and unreacted particles was observed for the L-glutamine. By 15 ms, RDX particles ejected from the sample surface started deflagrating as they reached the heated air above the sample surface (resulting in additional light emission and rapid vertical and horizontal expansion of the heated area).

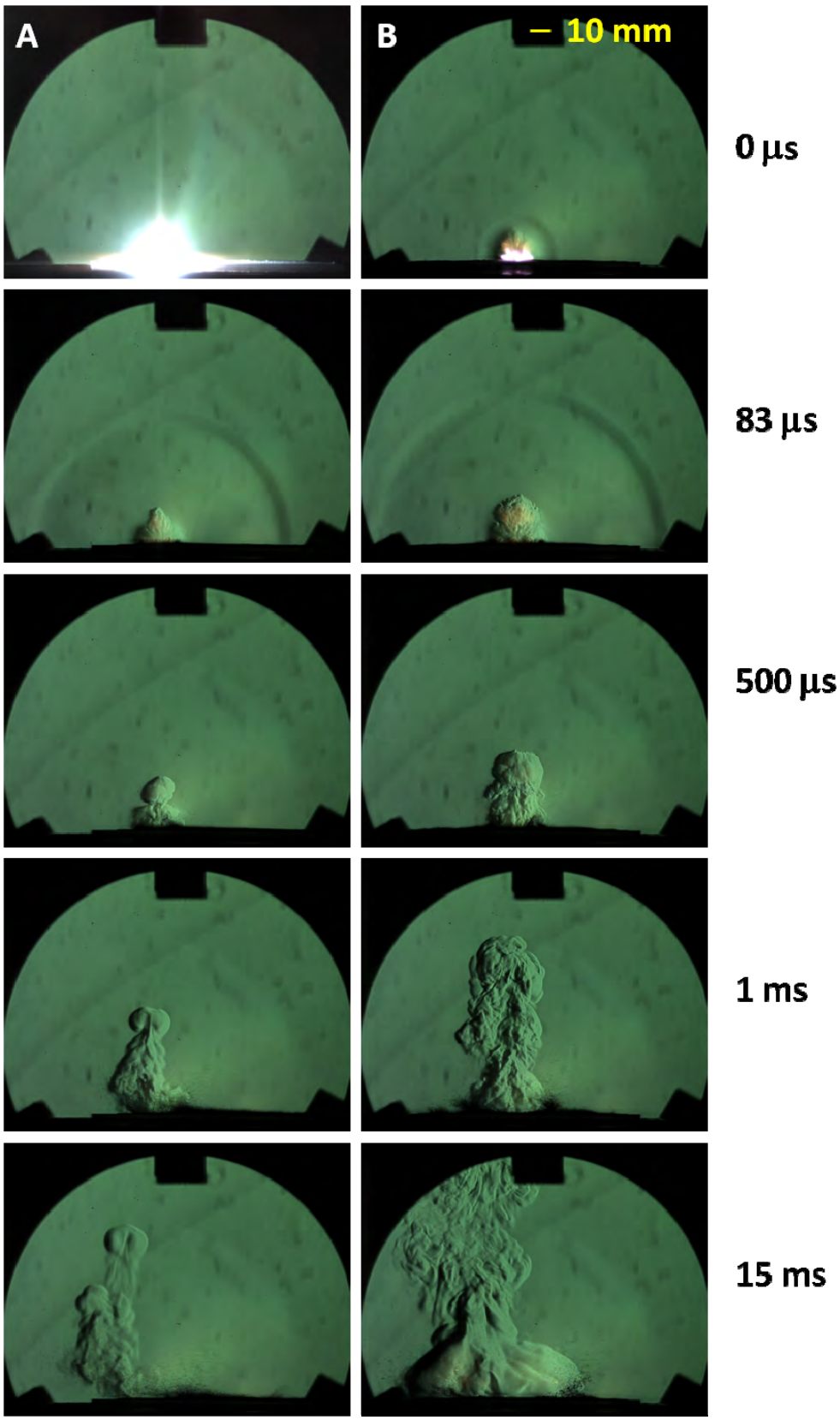

Figure 5. Schlieren images of laser-shocked (a) L-glutamine and (b) RDX.

3.2 Particle Ejection

Evidence for phase explosion can be seen in snapshots from the high-speed video for the laser ablation of the blank tape substrate (figure 6). Large pieces of the tape (579–925 μm) were observed moving away from the sample surface at slower velocities than the shock wave. This effect was only observed for the blank tape. A possible explanation is that the laser pulse passed through the tape (which is transparent to 1064-nm light), where heat was trapped between the glass slide and the back of tape, leading to explosive boiling.

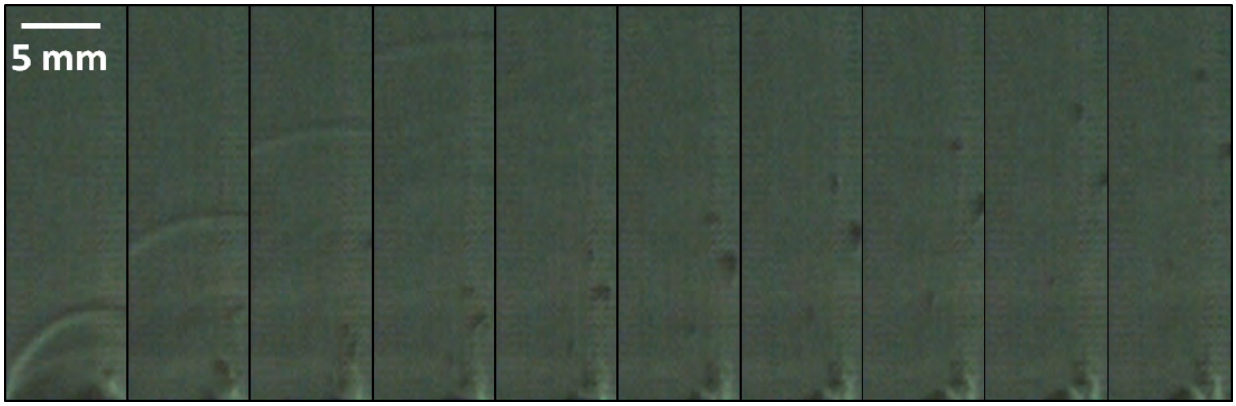

Figure 6. Snapshots of particles ejected from the blank tape substrate during the first 119 μs after the laser pulse. The observed particles range in size from 579 to 925 μm.

On the other hand, when a thin layer of energetic (or nonenergetic) material is affixed to the tape, most of the laser energy interacts with the material. This interaction, and subsequent interactions between the reflected internal shock wave and the sample surface, leads to ejection of the particles from the sample surface. Some of these particles are atomized in the laser-induced plasma. The remaining particles pass through the heated atmosphere, which can lead to combustion or deflagration in air (figure 7). The only nonenergetic sample observed to undergo laser-induced deflagration was sugar, when it was excited by two sequential laser pulses in a separate experiment (*49*). All the energetic material samples in this study (except for the granular black powder and smokeless gun powder) deflagrated.

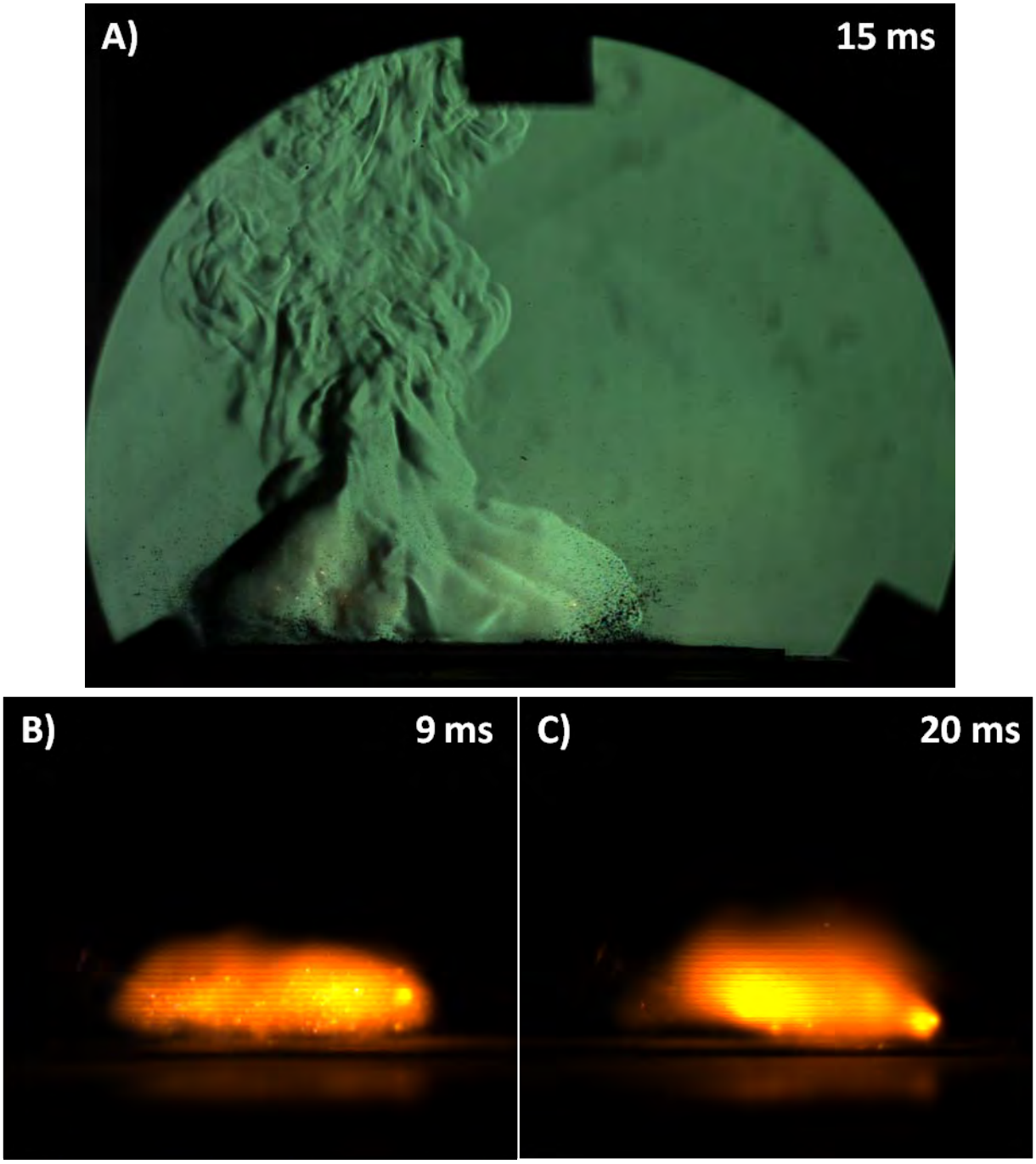

Figure 7. Images of the laser-induced deflagration of RDX: (A) schlieren image acquired 15 ms after the laser pulse (12,000 fps and 9.8-μs shutter); snapshots from direct video (42,000 fps and 23.8-μs shutter) at (B) 9 ms and (C) 20 ms.

3.3 Evidence for LSDW

LSDWs propagating toward the laser source have been observed in the shadowgraph images of laser-ablated brass targets in air (*40*) and aluminum targets in both air (*29*) and argon (*43*). Since at a maximum the LSDW lasts only as long as the laser pulse (6-ns duration in this experiment) and the distortion of the external shock front by the LSDW (caused by nonuniform heating of the central tip of the vapor plume) lasts less than 300 ns, direct observation of the LSDW was not possible with the current experimental setup; however, indirect evidence for the LSDW has been observed. Figure 8 shows several snapshots from the high-speed video (12,000 fps; 9.8-μs shutter) of the laser-ablated blank tape substrate. In the first frame, the shock wave (A) and plasma plume (C) were observed. In addition, a thin column of heated air (B) above the plasma plume was observed. This region is evidence for the presence of an LSDW during the laser pulse. As the plasma cools and the atomized and excited carbon combusts in the air (at times greater than 83 μs), the density gradient caused by the high-temperature plasma is no longer distinguishable from this region.

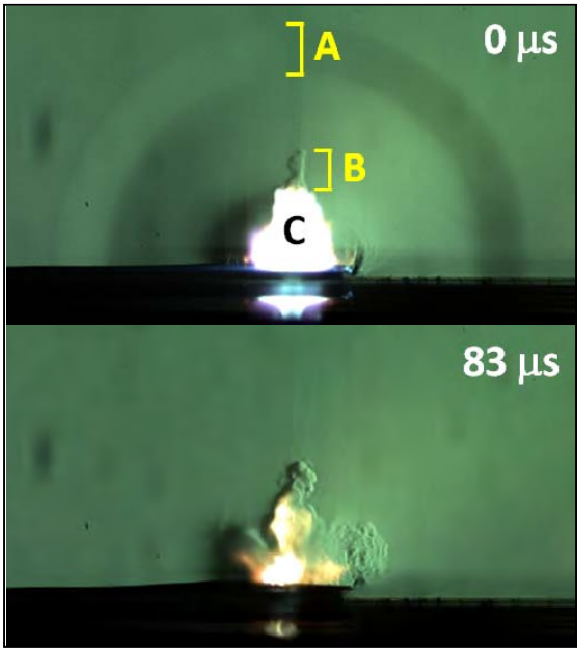

Figure 8. Snapshots from the laser ablation of the blank tape substrate showing the shock front (A), density gradient providing evidence for a LSDW (B), and the plasma volume (C).

High-speed video of the laser ablation of a solid titanium substrate was recorded (figure 9) with the laser normal to the target surface (A) and with the sample on a 30° incline (B). When the laser was perpendicular to the sample surface, a typical laser-induced plasma was observed. In the first frame after the laser ablation, the inclined sample shows a region of heated air in the direction

of the laser beam, while the laser-induced plasma and blast wave expand normal to the sample surface, as expected (figure 3). This provides additional evidence for the formation of an LSDW.

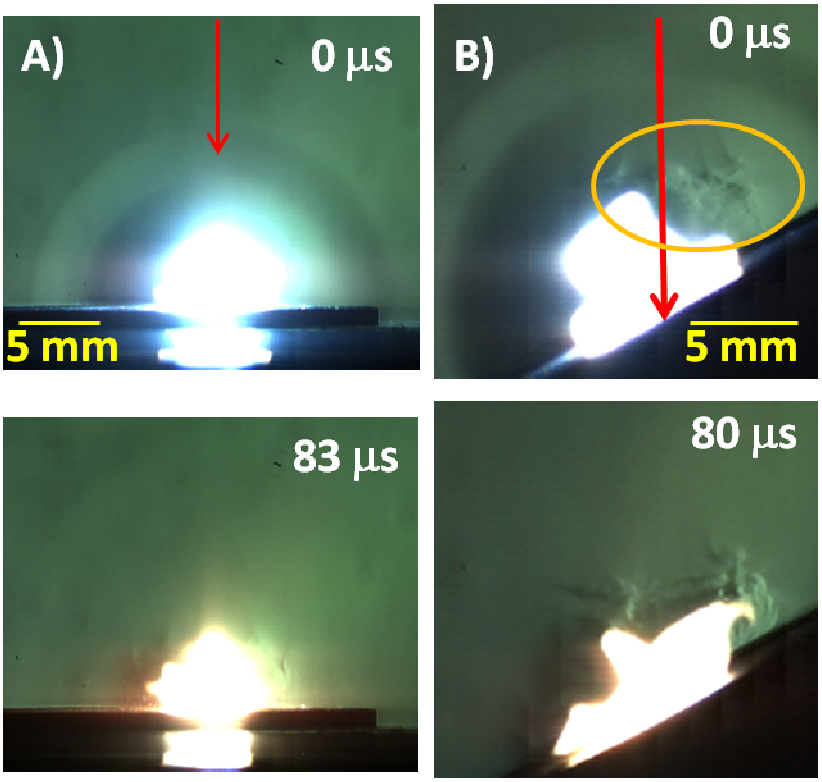

Figure 9. Snapshots of titanium substrate with the direction of laser propagation (A) perpendicular to the sample surface and (B) at a 30º angle to the sample surface (density gradient shows evidence for LSDW).

Finally, high-speed video of a black plastic substrate was obtained (figure 10) with the laser normal to the substrate (A) and with the sample on a 30° incline (B). Under some conditions, a faster-moving component of an expanding plume front can split into two clouds (plume splitting) (*9*). When the laser was perpendicular to the substrate, plume splitting was observed, while no plume splitting occurred with the sample on an incline. We postulate that the additional energy from the LSDW in the direction of the laser beam (coinciding with the propagation direction of the blast wave) resulted in the observed plume splitting (figure 10A). These results, in combination with the relatively high laser fluence (table 2) and heated regions of air surrounding the location of the laser beam, suggest that an LSDW was present at very early times under the current experimental conditions and likely influenced the plasma chemistry and shock formation.

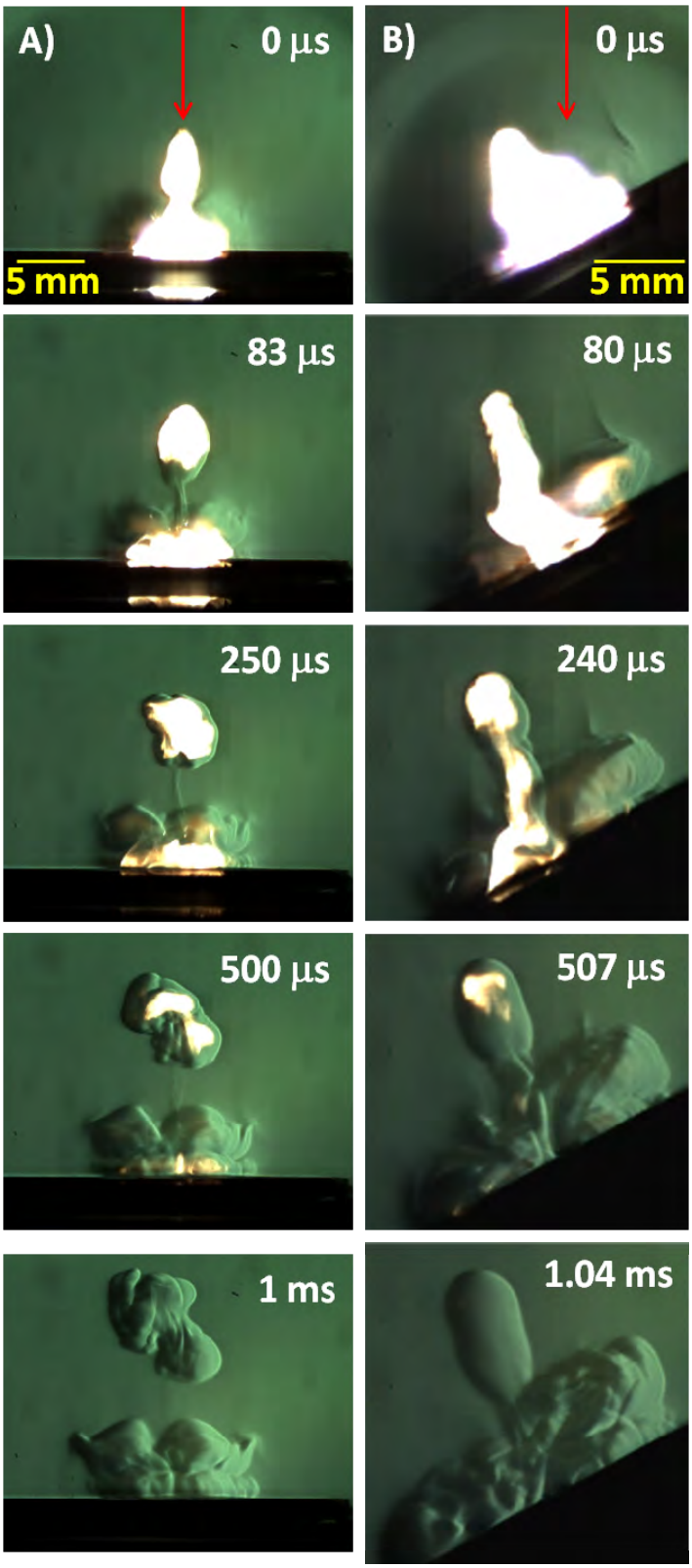

Figure 10. Black plastic evidence for LSDW (more energy from ejected particles when laser coincides with blast direction).

3.4 Shock Front Propagation

Multiple shock fronts have been identified in the literature for laser-ablated materials. In addition to the LSDW travelling at Mach 3, Maher and Hall (*24*) observed a second wave travelling near Mach 1 (which they postulated was from the sample material vaporization) and a third wave travelling near Mach 0.5. Callies et al. (*21*) observed multiple discontinuities, which they attributed to the kinetic energy of the evaporated material accelerating the ambient gas, the contact front between the plasma and the shocked air, the contact front between the evaporated material and the shocked gas, the interface between the target material and the air, and the high-temperature plasma region. Wen et al. (*54*) used femtosecond shadowgraphy to track what they described as an internal shock wave, an external shock wave, an LSDW, and a laser-supported combustion wave. Harilal et al. (*43*) observed a primary shock followed by a secondary shock that they attributed to the internal shock-wave structure within the plasma plume.

When the outward-moving external shock wave forms, an internal shock wave develops to balance the velocity and high backpressure generated by the external shock wave when the vapor plume expands supersonically; this internal shock wave propagates back toward the target surface. When the internal shock impacts the target surface, it is split into two shocks: one travels through the target material and another propagates back toward the main external shock; when the internal shock wave catches up to the contact surface, it is reflected back toward the target surface again. This reflection-transmission phenomenon can repeat multiple times, generating new refracted external shocks (*8, 63*). Because the target in this experiment is a thin layer of material affixed to transparent tape on a glass slide, a strong enough internal shock could also transmit through the sample until it hits the vertical stage and is reflected back toward the external shock by the sample stage.

Figure 11 shows the first 15 frames from the high-speed video (84,000 fps; 1-μs shutter) from the laser ablation of the blank tape substrate (A and B), L-glutamine (C), and RDX (D). The initial frame captures the first microsecond of the event, and each successive frame is 11.9 μs later; the first 15 frames thus capture the first 178.5 μs (at later times the external shock has travelled outside the field of view of the 10.8-cm schlieren mirrors). In (A), the camera was focused in front of the laser-induced plasma (33 cm closer to second mirror) to optimize visualization of the three shock fronts (1–3). The dark band is the expanding external shock front, while the light band immediately following the main shock front is a result of refracted light rays. Two additional shock fronts were observed at later times. In (B), the camera was focused on the laser-induced plasma so that the expansion of the plume (4) and the expansion of the column of heated air from the LSDW (5) could be tracked. The plume expansions of L-glutamine and RDX are shown in (C) and (D), respectively. The shock front and luminous region above the laser-induced plasma in the first frame of (C) are artifacts due to the reflection of a small region of air breakdown above the focusing lens for the laser.

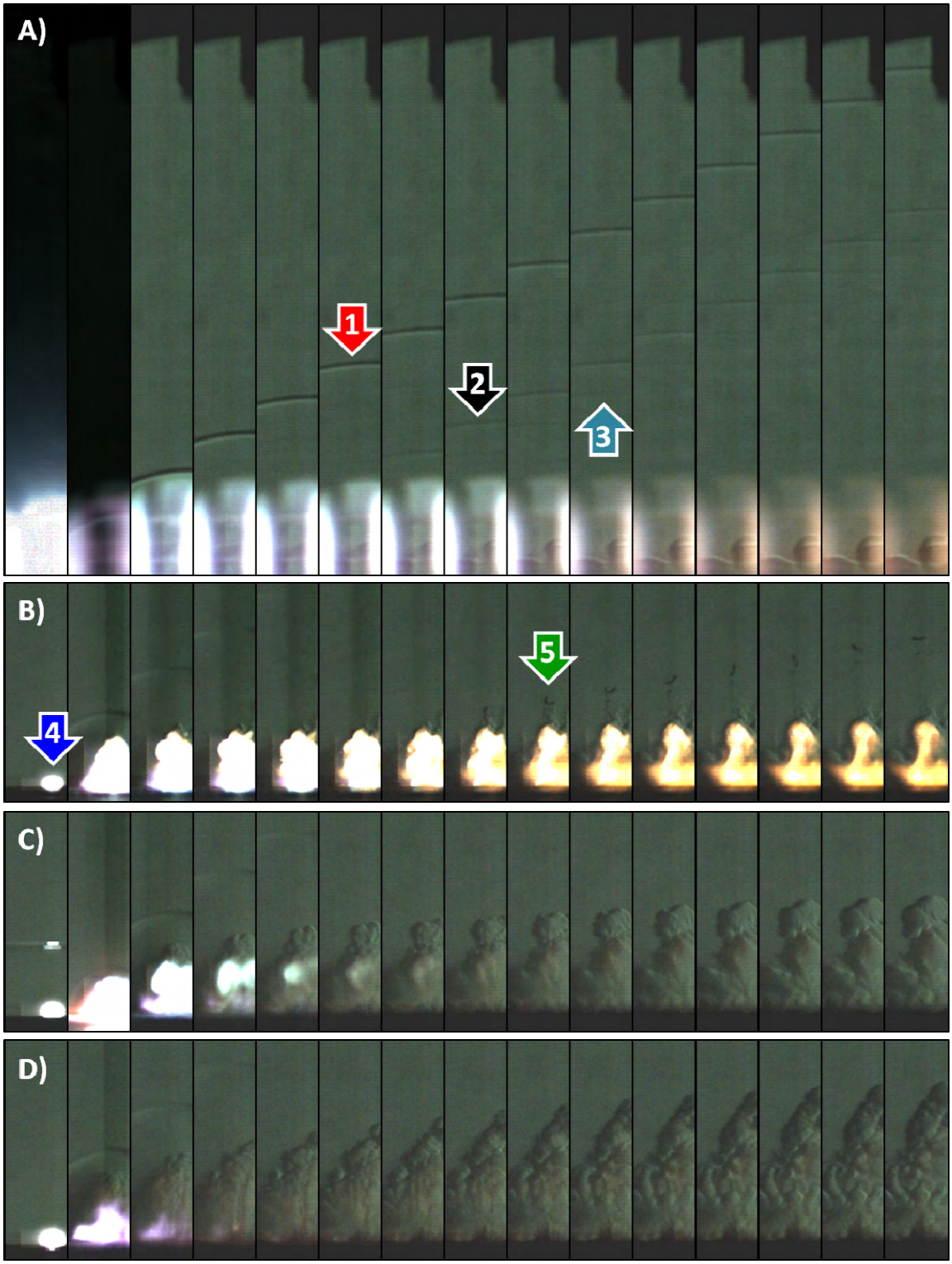

Figure 11. First 15 frames from the high-speed video from the laser ablation of : (A) blank, focus in front of plasma; (B) blank, focus on plasma (1 = primary shock front, 2 = second shock front, 3 = third shock front, 4 = plasma front, 5 = density gradient extending away from target surface toward the laser); (C) L-glutamine, focus on plasma; (D) RDX, focus on plasma.

The position-time plot (*R-t*), or time line, for the plasma plume position, density gradient position, and shock front positions for the blank tape substrate are shown in figure 12. The main external shock wave was not observed until about 8 mm above the target surface because of the strong plasma emission. After about 80 μs, a second shock front was observed; a third appeared after approximately 90 μs. The shock time line for a nonenergetic sample (figure 13), L-glutamine, was very similar despite a significant difference in plasma luminosity at later times (figure 11C). The second and third shock fronts appeared earlier (60 and 70 μs, respectively), and the region of heated air above the plasma plume was larger. The shock time line for an energetic sample (figure 14), RDX, looked quite different. The laser-induced plasma was significantly less luminous, and all visible emission was gone after 85 μs (this general trend was observed for all energetic materials, see section 4.2). The heat-affected zone above the laser-induced plasma was extremely large compared to the blank and L-glutamine. The second and third shock fronts appeared much earlier at 35 μs, and fourth and fifth shock fronts appeared after 60 μs.

Unfortunately, with this experiment it was not possible to definitively determine the origin of the additional shock fronts; however, their presence is likely indicative of the extra energy released during the laser ablation of an energetic material and the subsequent exothermic reactions in the laser-induced plasma (*15*). For example, a strengthened internal shock wave would undergo more internal reflections and generate stronger refractive shock fronts. The external shock wave velocity was also faster for the energetic material, as discussed in section 3.5. Although the velocity of the shock wave decreases with each successive frame (approaching the speed of sound in air at 343 m/s), the laser-induced shock wave had not yet decayed into a sound wave by the final camera frame for any of the samples.

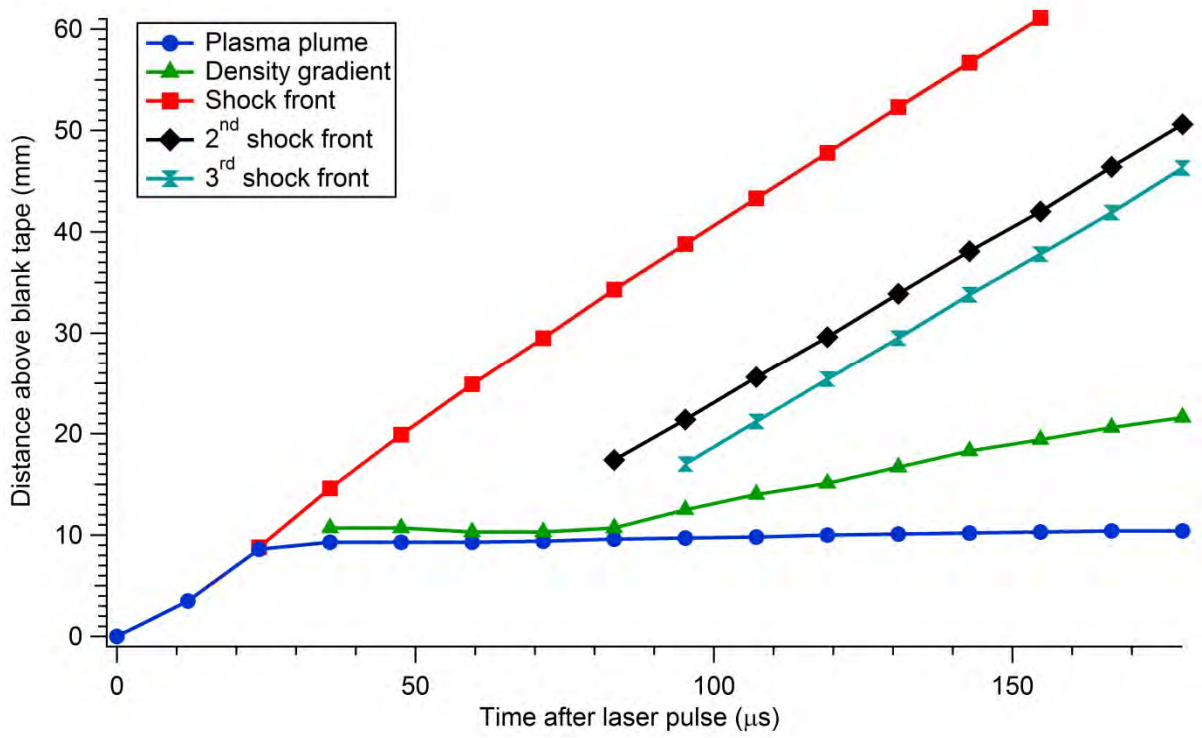

Figure 12. Blank shock time line.

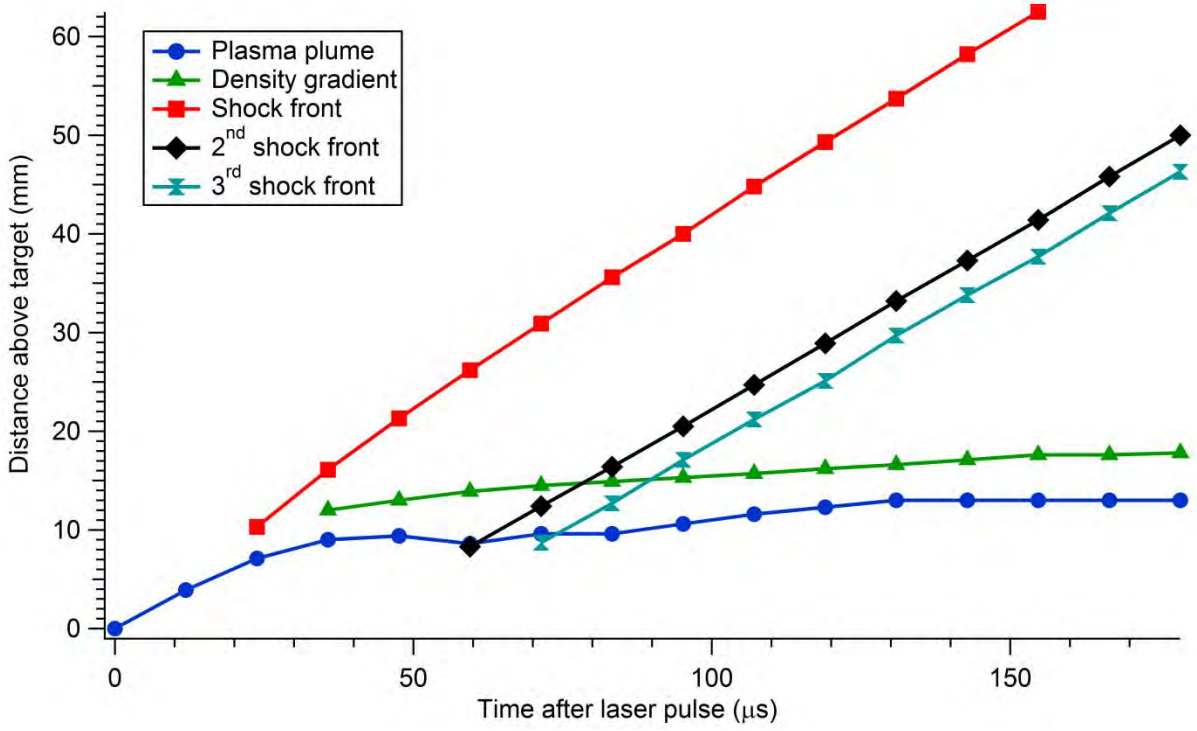

Figure 13. L-glutamine shock time line.

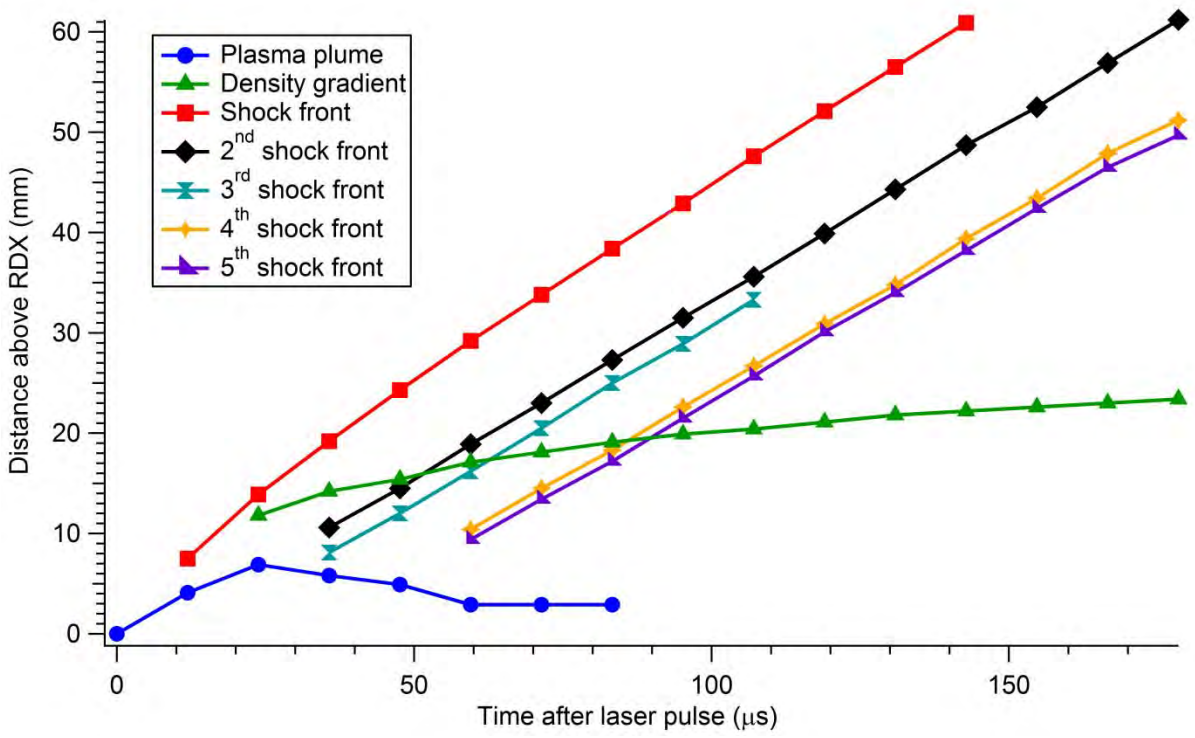

Figure 14. RDX shock time line.

3.5 Measurement of Shock Velocities

Typically expansion velocities are determined by the derivative of the position-time graph, where the data is fit to a model based on classical point blast theory. Most papers that measure the laser-induced shock wave apply the Sedov-Taylor relationship (equation 1), which predicts an exponential factor of 0.4. Figure 15 shows the fits for both energetic and nonenergetic materials to an equation of the form $R = At^q$. The goodness of each fit is indicated by the χ^2 statistic, which is given by

$$\chi^2 = \sum \frac{(y - y_i)^2}{\sigma_i^2} \tag{8}$$

where y is the fitted value for a given point, y_i is the measured data value for the point, and σ_i^2 is an estimate for the standard deviation of y_i. A smaller value of χ^2 indicates a better fit.

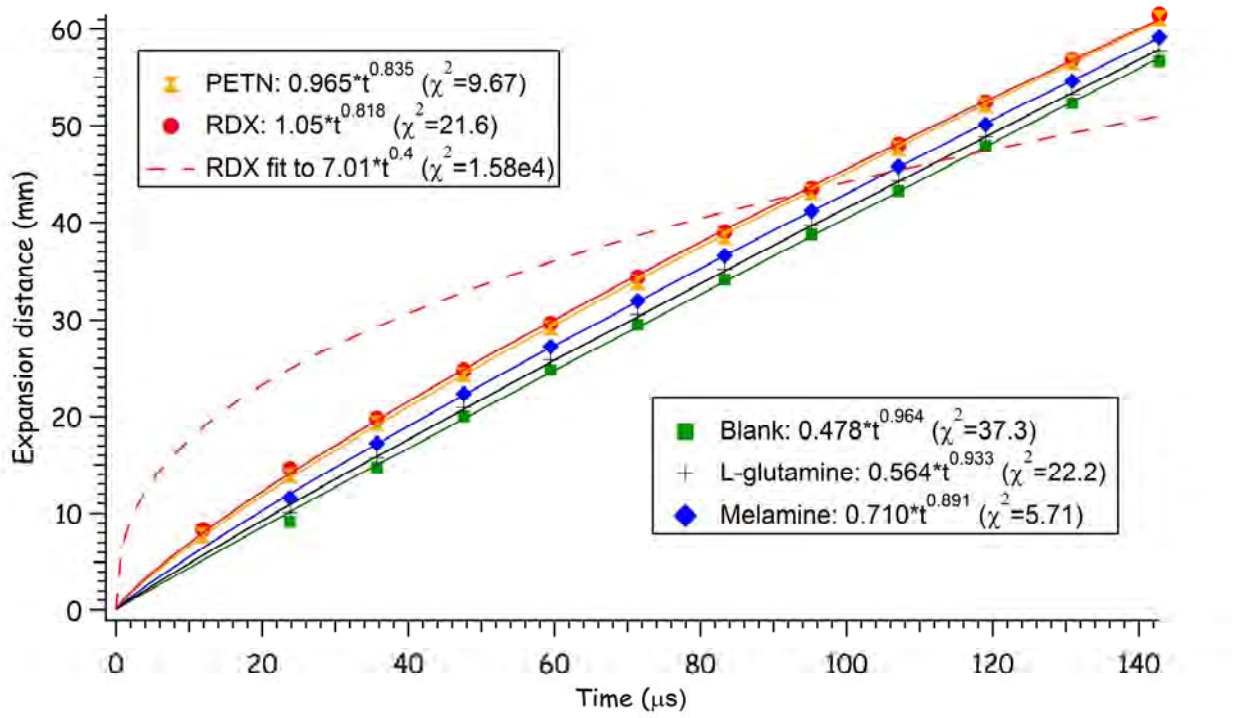

Figure 15. Expansion distance of the shock waves vs. time demonstrating that the Sedov-Taylor relationship ($\sim t^{0.4}$) is not valid at these distances.

While a power function describes the expansion distance of the shock waves versus time reasonably well, the exponential factor q is much higher than 0.4 (close to 0.9 for the nonenergetic materials and 0.8 for the energetic materials). Classical point blast theory assumes energy is instantaneously released into the surrounding atmosphere from an essentially massless point source, forming a spherical shock wave (*18*). This neglects the effect of exothermic reactions occurring after the initial laser pulse. In addition, the strength of the blast wave must be sufficiently large enough to neglect the ambient gas pressure in comparison with the pressure behind the shock wave—an assumption that is not valid at longer distances when the shock wave begins to decay. The treatment of weak shock waves requires inclusion of source mass (*64*) or counterpressure (*22*)—approximate expressions that need to be solved numerically. Although many previous studies have successfully applied the Sedov-Taylor theory to laser-induced shock waves, most used nonreactive materials and observed the shock wave at shorter timescales (less than 1 μs).

Previous studies have shown that decreasing the atmospheric pressure (e.g., *9*, *30*, *33*) or using a laser spot size of the same magnitude as the measured shock wave distance (*65–69*) can result in higher exponents. In this experiment, the diameter of the focused laser was 0.8 mm, and the first image of the shock wave was obtained 8 mm above the sample surface. Only a few papers have reported $q > 0.4$ at standard pressure. Srinivasan et al. (*68*) reported an exponent of 0.76 for the shock wave expansion of a laser-ablated organic substrate, polymethylmethacrylate.

No explanation for the deviation from Sedov-Taylor theory was given. Schmitz et al. (*42*) attributed the higher exponents obtained for various organic materials (0.48–0.68) to the relatively low laser fluences (<1.0 J/cm^2) used in their experiment; this explanation would not apply to the current experiment. If the dynamics of the shock front are determined by the volumetric gain of particles caused by the change in their density during the transition from the condensed to the vapor state and the subsequent heating of the plasma resulting from absorption of laser radiation, then the Sedov-Taylor scaling is not applicable (*20*). In the current experiment, the presence of the LSDW and the significant plasma shielding that occurs with a 1064-nm pulse at 900 mJ result in significant plasma heating.

While classical Sedov-Taylor blast wave theory is only valid when the energy behind the shock wave comes from a point source, variants of the theory have been developed to account for the mass contribution of the point source (*64*, *69*). Following this approach, when the shock wave radius is fit to a power law dependence of the form

$$\mathrm{R}(t) = At^{\alpha} \tag{9}$$

the time-dependent energy takes the approximate form

$$R(t) = \frac{8\pi\rho_0 (3\gamma - 1)}{(3\gamma + 1)^2 (\gamma - 1)} A^5 \alpha^2 t^{(5\alpha - 2)} \tag{10}$$

where ρ_0 = 1.20 kg/m^3 and γ = 1.4 for the density and specific heat capacity of the unshocked air, respectively, and A and α are the fitting parameters from equation 9. Using equation 10 and the fits shown in figure 15 result in the time-dependent energies for the inert and energetic samples shown in figure 16. This treatment assumes that the contribution of the solid-phase particles is negligible over the observed timescale, and that the heat capacities for the laser-ablated material and ambient gas are equivalent; the absolute magnitudes of the estimated energy release have previously been shown to be unrealistic (*45*), although in that case the calculated energies were significantly higher than the energy put into the system with the ablation laser. The estimated energy values do, however, enable comparison of the relative magnitudes of energy release for each sample. The energy release from the energetic samples is much more significant than for the nonenergetic samples at t > 10 μs; only the energetic samples undergo exothermic combustion reactions leading to eventual deflagration (after several milliseconds).

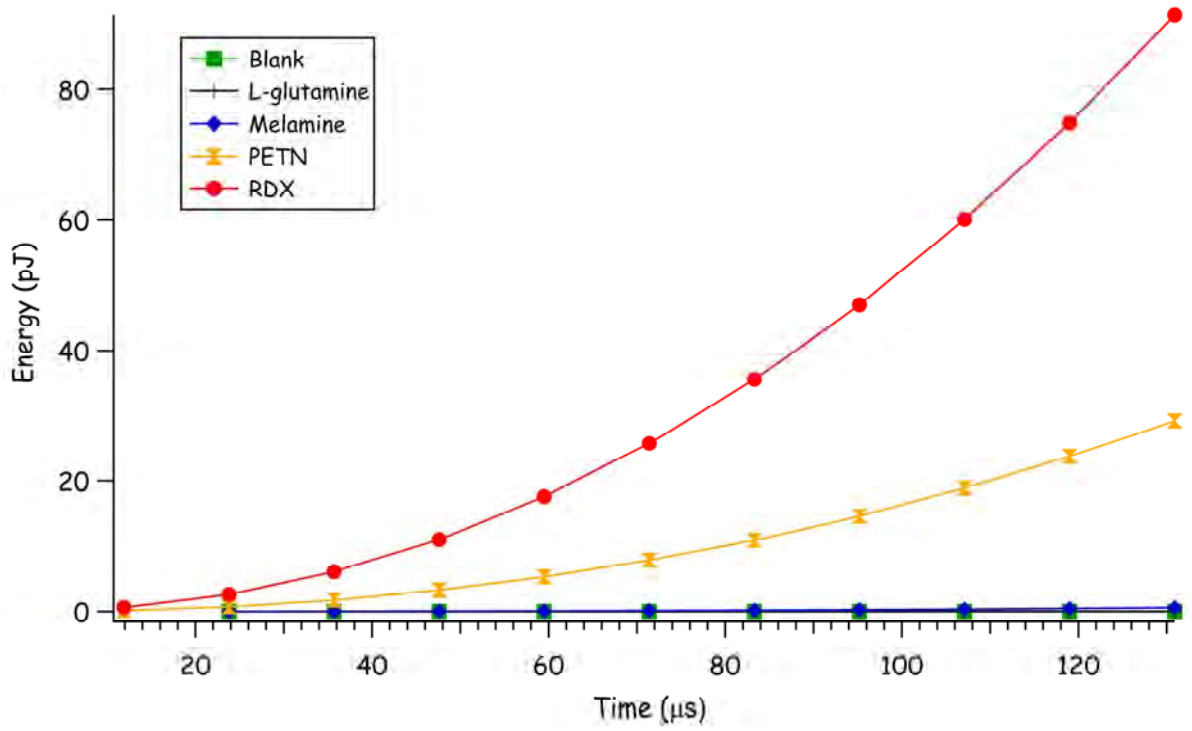

Figure 16. Calculated time-dependent energy release for energetic and nonenergetic samples.

A second model that is often applied to laser-induced shock fronts at longer distances is the drag model (equation 2). Figure 17 shows the fits for the expansion data to the drag model. While the model fits reasonably well to the nonenergetic samples, the fit to the energetic samples is extremely poor. The drag model underpredicts the shock velocity for the energetic materials at times less than 50 μs—further indication that additional energy is put into the plasma by the exothermic reactions.

Dewey (*70*) fit the shock position versus time for a large-scale TNT detonation (500 ton) to the equation

$$R = A + Bt + Cln(1+t)+D(ln(1+t)\ )^{1/2} \qquad (11)$$

where *A*, *B*, *C*, and *D* are fitted coefficients, and *R* and *t* are the shock radius and time, respectively. As shown in figure 18, the explosive samples RDX and PETN fit very well to equation 11 with $R \approx 0$ at $t = 0$. The fits for the inert materials, on the other hand, predicted a negative shock radius at $t = 0$. For all samples, $\chi^2 < 1$ indicates that the model is overfitting the data. Thus, while equation 11 works relatively well for laser-shocked energetic materials, it is not appropriate for the inert materials.

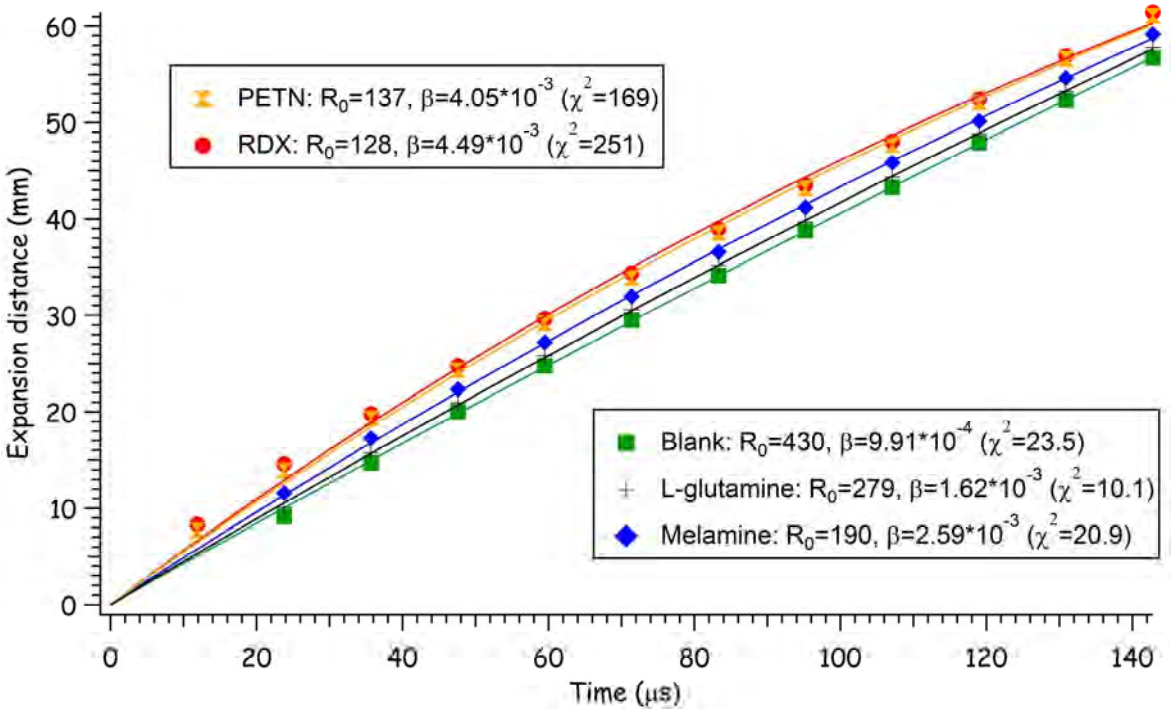

Figure 17. Expansion distance of the shock waves vs. time demonstrating that the drag model is not valid at these distances.

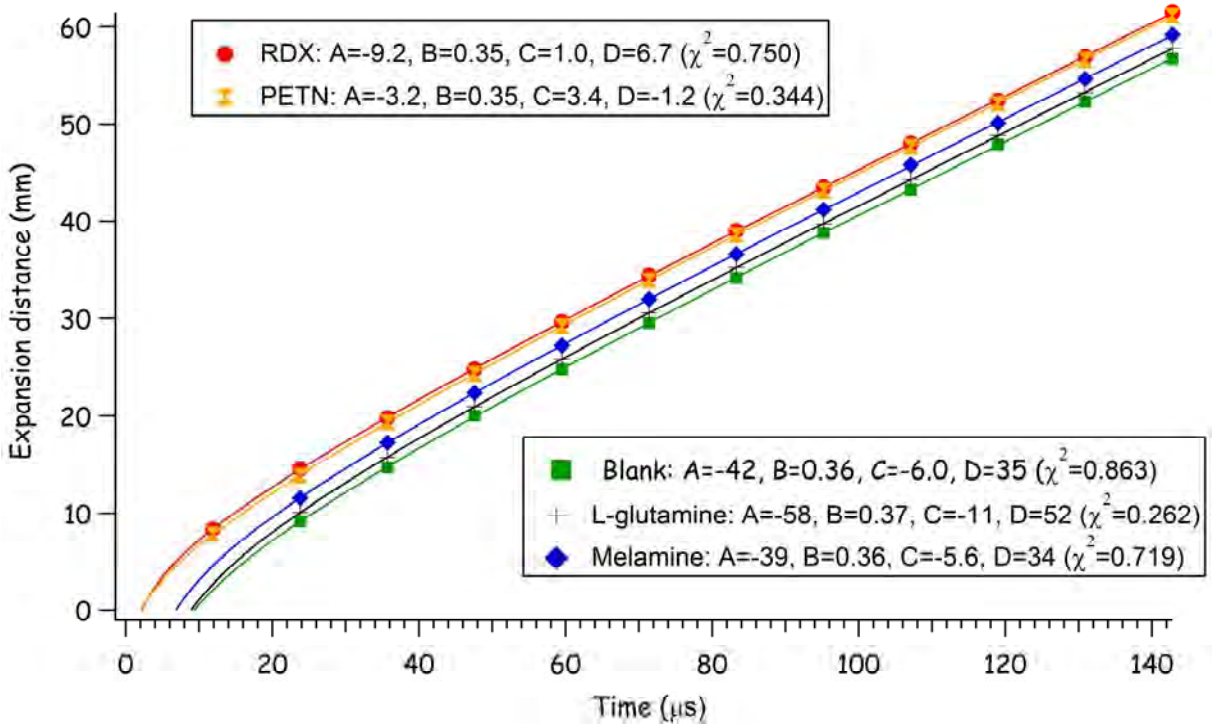

Figure 18. Expansion distance of the shock waves vs. time fit to the Dewey equation (*11*).

In order to simplify the data analysis and avoid having to fit the samples to different models depending on whether they were energetic or not, the velocity versus time plot for each sample was fit to a fifth-order polynomial (figure 19). A fifth-order polynomial was selected to fit the shock data as a compromise between the precision of the measurement (which increased with lower-order polynomials) and the quality of the fit (which increased with higher-order polynomials). The characteristic air shock velocity for each sample was defined as the y-intercept. The actual velocity of the shock wave at very early times (nanosecond timescale) is on the order of kilometers per second when it is being accelerated by the supersonic expansion of the plasma plume. Here, the y-intercept does not reflect the velocity at time zero but at the point in time when the shock front expands freely into the ambient air without additional energy input from the plasma or subsequent chemical reactions. As shown in figure 19, the characteristic air shock velocities (from one laser shot) of PETN (833 m/s) and RDX (801 m/s) are significantly higher than those of the inert materials (562–604 m/s).

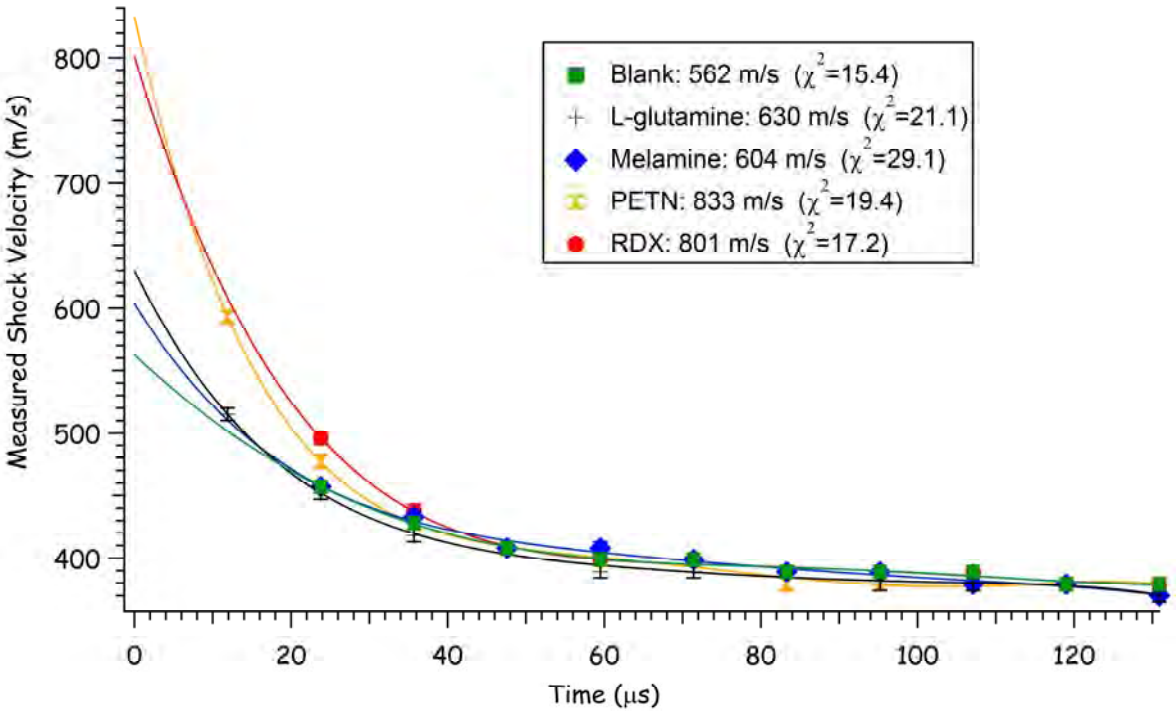

Figure 19. Measured shock velocity vs. time with fifth-order polynomial fits.

3.6 Correlation Between Laser Pulse Energy and Shock Velocity

The characteristic air shock velocity was measured for the blank substrate at a variety of laser pulse energies to determine the effect of the input laser energy on the shock front at the measured distances (figure 20). The error bars represent the 95% confidence intervals for a limited data set of five laser shots each. The data fit reasonably well to a linear regression fit, except for the first data point at E_p = 220 mJ. The relationship between the shock radius and the laser pulse energy can be described by

$$R(E) = BE^{\alpha/2} \quad (12)$$

where B and α are the fitting constants (*42*). As before, the ideal spherical shock wave would yield $\alpha = 0.4$. A fit of the data to a power law dependence resulted in an improved R^2 value with $\alpha = 0.3$.

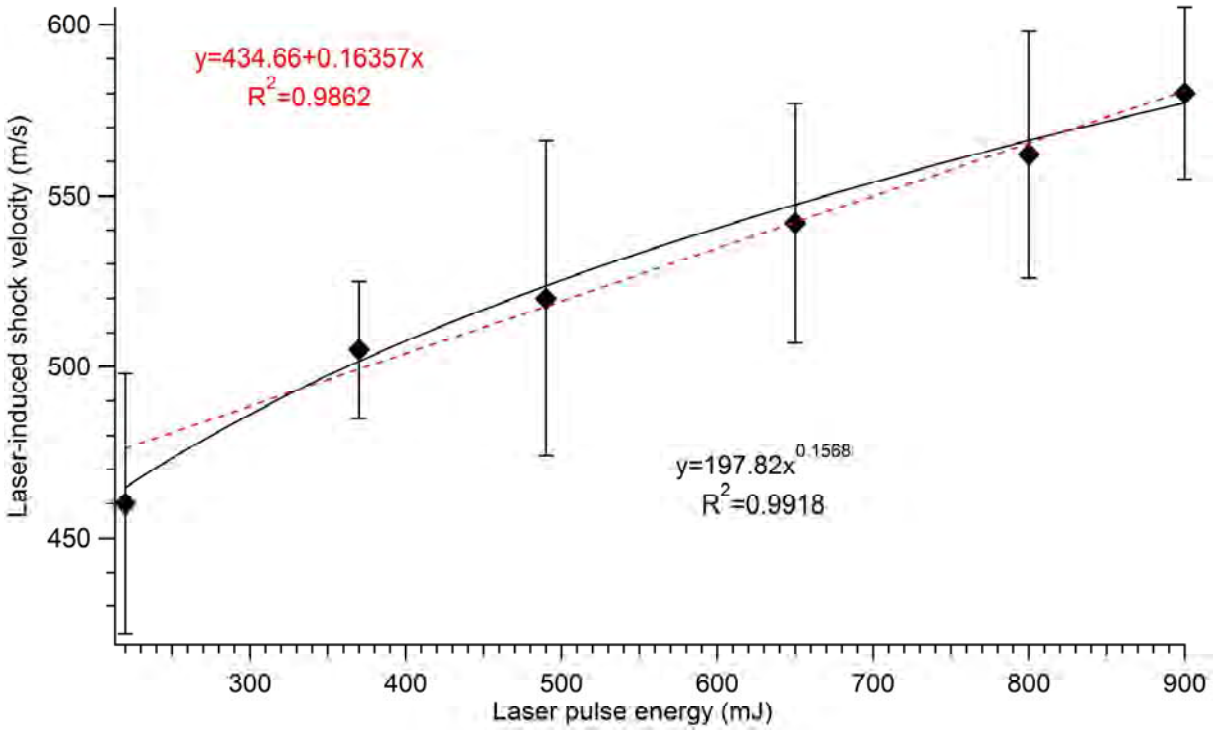

Figure 20. Relationship between the laser-induced air shock velocity and the laser pulse energy.

3.7 Conversion to Shock Pressure

The peak air shock pressures for the blank, L-glutamine, and RDX samples were calculated using equation 7. Near the center of a blast, the pressure is proportional to R^{-3}, while at great distances from the explosion center the pressure decays as R^{-1}, as in a sound wave (*18*). While the pressure from the inert samples decays as R^{-1} for expansion distances greater than 10 mm (figure 21), the pressure from RDX decays as R^{-2}, indicating excess pressure for the energetic material beyond that imparted by the initial laser "explosion."

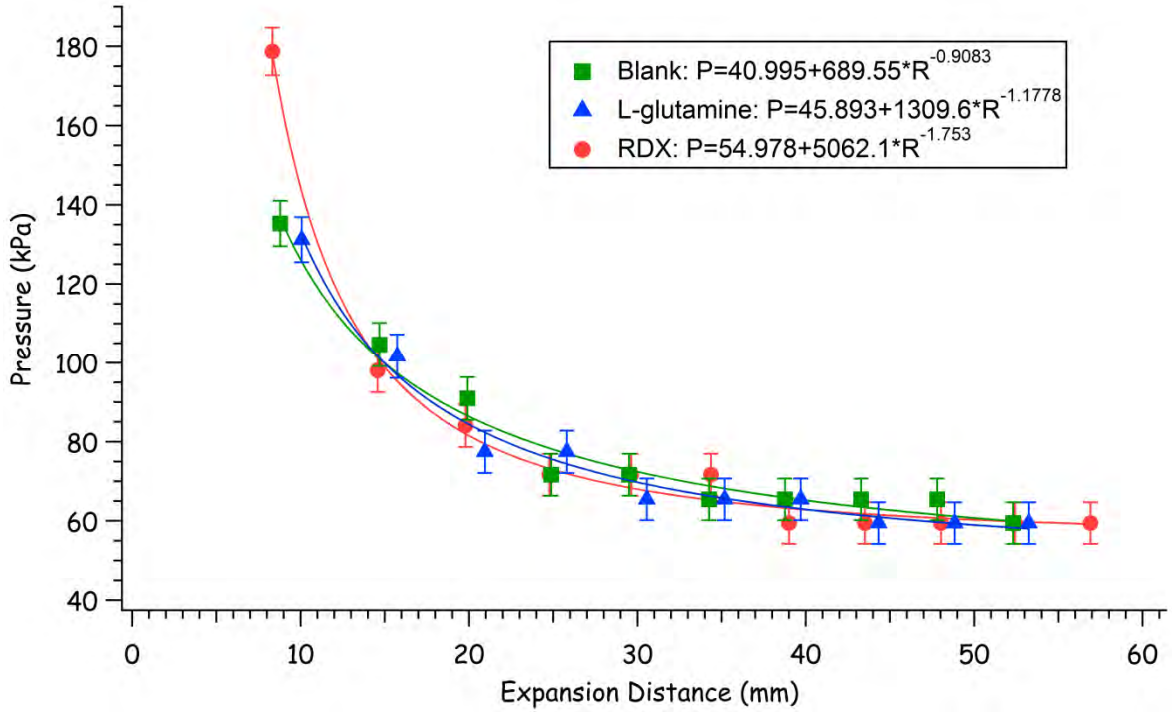

Figure 21. Relationship between the laser-induced air shock pressure and the expansion distance.

4. Energetic Material Performance

4.1 Nonenergetic Materials vs. Energetic Materials

The most obvious difference in the high-speed videos of the laser-material interaction between nonenergetic (inert) materials and energetic materials is the luminosity of the plasma emission. Inert materials result in an intensely brilliant white light for the first camera frame (figure 22); the resulting shock front is clearly visible in subsequent frames. Light emission from the graphite (B–D) and diamond (H) samples continues for several frames (although the camera focus is in front of the laser-induced plasma). Plasma lifetimes for most materials last hundreds of microseconds with a 900-mJ focused laser at 1064 nm.

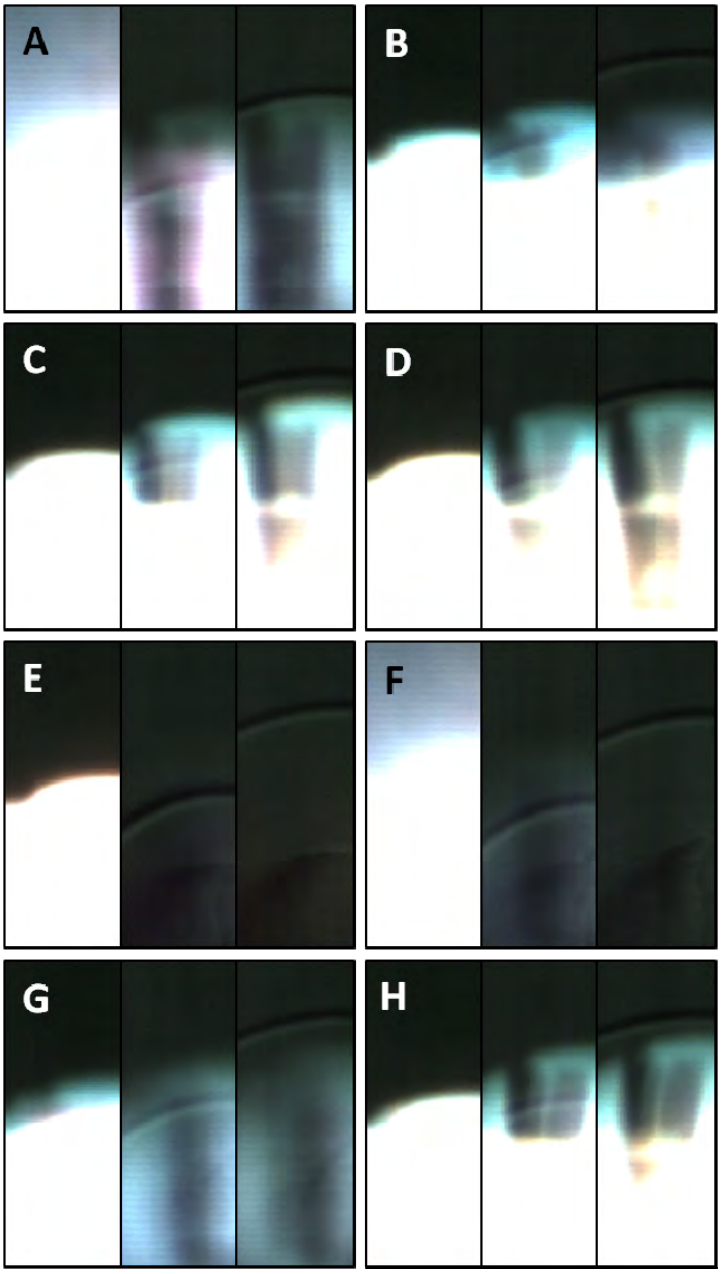

Figure 22. Light emission from nonenergetic materials: (A) blank tape, (B) micron-sized graphite, (C) GNP, (D) NG, (E) sugar, (F) L-glutamine, (G) melamine, and (H) micron-sized diamond grit.

Light emission from the energetic materials looks distinctly different (figure 23). Because of the decreased plasma luminosity, the shock front is observable from the first camera frame for all energetic materials. Differences in the emission wavelengths observed by the camera are due to chemical reactions, e.g., the addition of 1.5% stearic acid to RDX results in an increase in visible emission (D) compared with pure RDX (G).

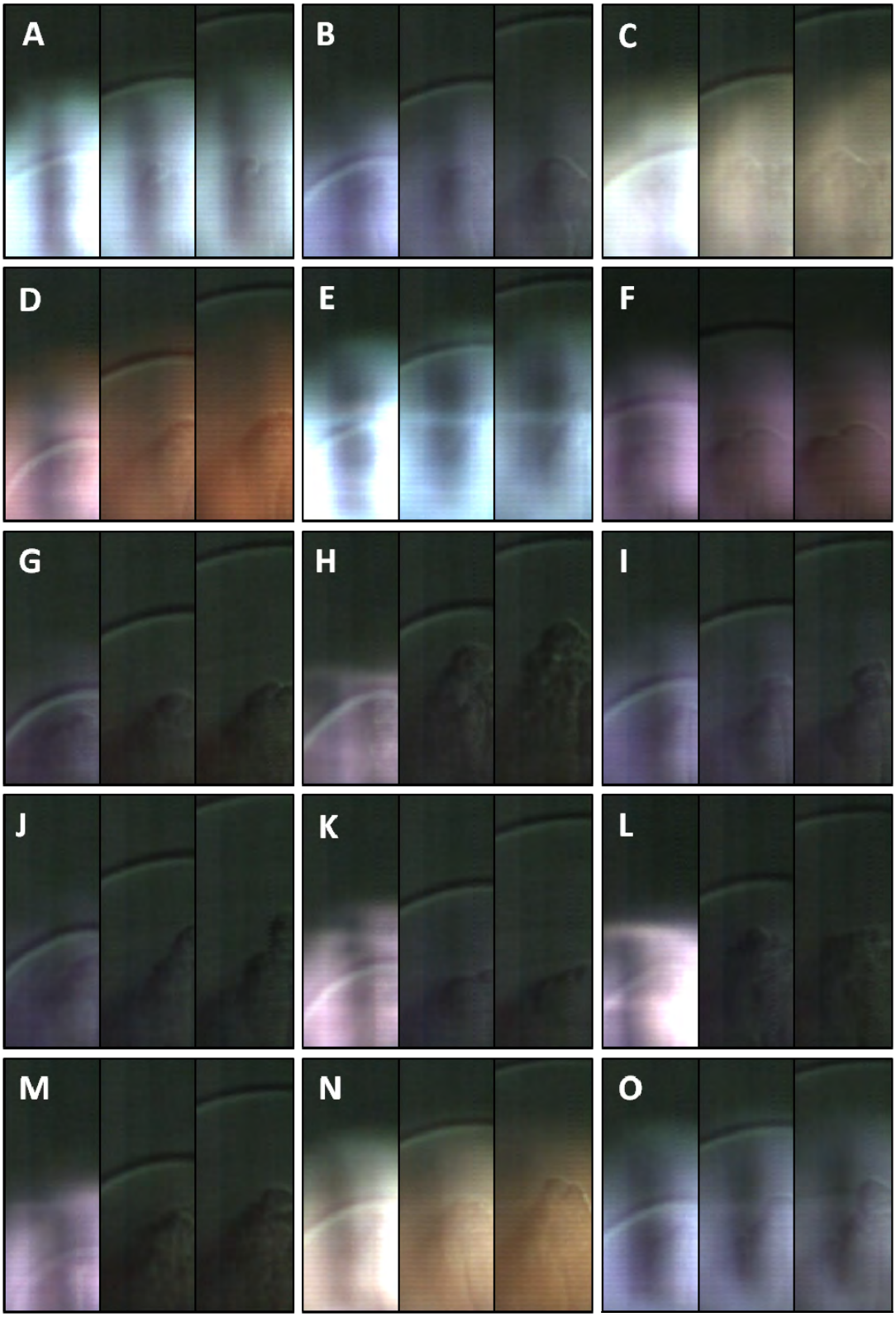

Figure 23. Light emission from energetic materials: (A) m-DNB, (B) TNT, (C) HNS, (D) Comp-A5, (E) p-DNB, (F) TATB, (G) RDX, (H) Pentolite, (I) Comp-B, (J) HMX, (K) PETN, (L) CL-20, (M) TAG-MNT, (N) H_2bta, and (O) HBT.

4.2 Chemically Reactive Materials

Chemical reactions result in distinct emission for several nonenergetic samples (figure 24), including the Epsom salt (green emission in A) and AN (orange emission in B). Magnesium sulfate is a naturally occurring, hygroscopic inorganic salt used to manufacture explosives and matches. Magnesium sulfate and atomized magnesium atoms will react via the exothermic reaction (*71*)

$$MgSO_4 + 4\,Mg \rightarrow MgS + 4\,MgO\,. \tag{13}$$

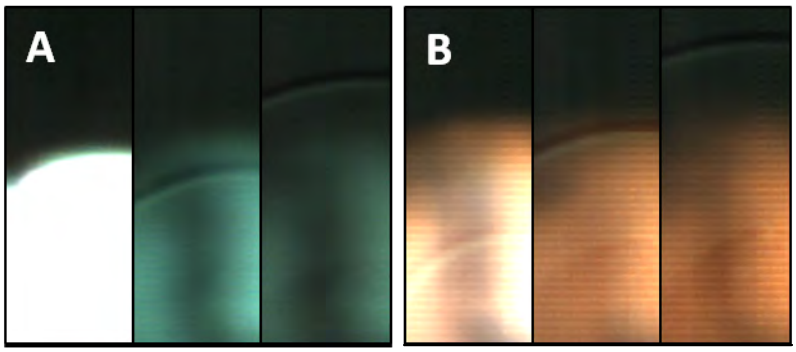

Figure 24. Light emission from chemically reactive materials: (A) Epsom salt ($MgSO_4$) and (B) AN (NH_4NO_3).

The green system of magnesium oxide (MgO) $\left(B\ ^1\Sigma - X\ ^1\Sigma\right)$ results in light emission from 476 to 521 nm (*72*). AN is a poor explosive by itself because it is overoxidized and extremely difficult to initiate; it is used safely as a fertilizer in multitonnage quantities but is also an effective explosive when mixed with a suitable fuel. Upon heating, AN will decompose according to the exothermic reactions (*73*)

$$NH_4NO_3 \rightarrow N_2O + 2\,H_2O \tag{14}$$

$$NH_4NO_3 \rightarrow N_2 + 0.5\,O_2 + 2\,H_2O \tag{15}$$

In the presence of a fuel, the following exothermic reaction occurs:

$$2\,NH_4NO_3 + C \rightarrow 2\,N_2 + CO_2 + 4\,H_2O \tag{16}$$

The tape may provide a limited fuel source for the AN reaction. The first positive system of N_2 $\left(B\ ^3\Pi_g - A\ ^3\Sigma_u^+\right)$ has strong emission near 580 nm (*72*).

A comparison of the high-speed video from two propellants, black powder and smokeless gun powder, is shown in figure 25. Unlike the other energetic materials in this study, black powder and smokeless gun powder are granular composite propellants consisting of a fuel and oxidizer. Black powder consists of a combination of carbon (charcoal), sulfur, and potassium nitrate. Smokeless powder formulations usually contain nitrocellulose and may also contain deterrents (to slow the burning rate), stabilizers (to prevent or self-decomposition), flash reducers (to

reduce the brightness of the muzzle flash), and/or other additives. The smokeless powder formulation (B) shows reduced light emission upon laser excitation compared to the black powder (A), which makes it easier to visualize the shock front.

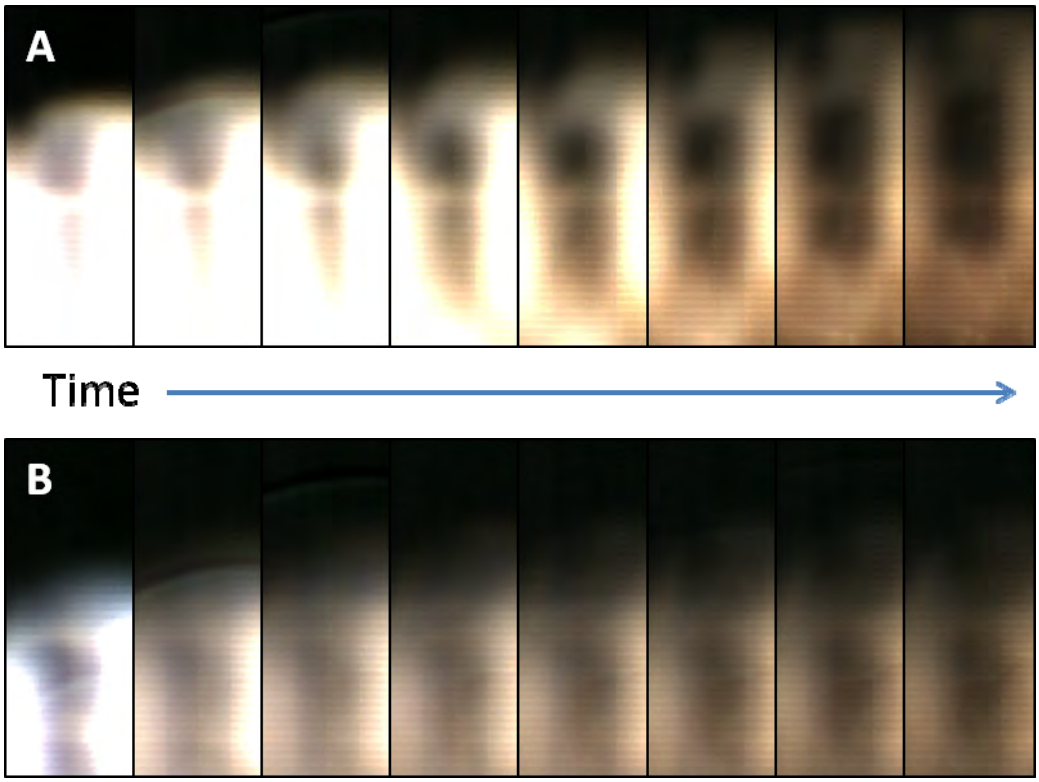

Figure 25. Light emission from (A) black powder and (B) smokeless powder.

4.3 Correlations Between Shock Velocities and Explosive Properties

The characteristic air shock velocities for each of the samples in table 1 were determined as described in section 3.5 and converted to shock pressure with equation 7; the results are shown in figure 26. The error bars represent 95% confidence intervals and reflect the shot-to-shot variations common with the laser ablation of powdered materials (*11*, *74*) and the relatively limited number of laser shots (5–8) recorded for each sample. The lowest air shock pressures were obtained for the inert materials, including the blank substrate, carbon samples, sugar, L-glutamine, and melamine. It has previously been observed that the repulsive force from a hard sample increases the shock wave velocity, while softer samples absorb the recoil energy of the ablated atoms, subsequently decreasing the speed of the shock wave (*75*). However, with high laser fluencies, the recoil force exerted on the surface by the expanding vapor is minimized, and the relative hardness of the material is less important (*3*). A comparison of the measured air shock pressures for the graphite samples (graphite, GNP, NG) with the diamond shock pressure shows that although the increased hardness of diamond does increase the shock pressure, the addition of energy to the plasma through chemical reactions produces much more significant increases in shock pressure (e.g., Epsom salt and AN have significantly higher shock pressures).

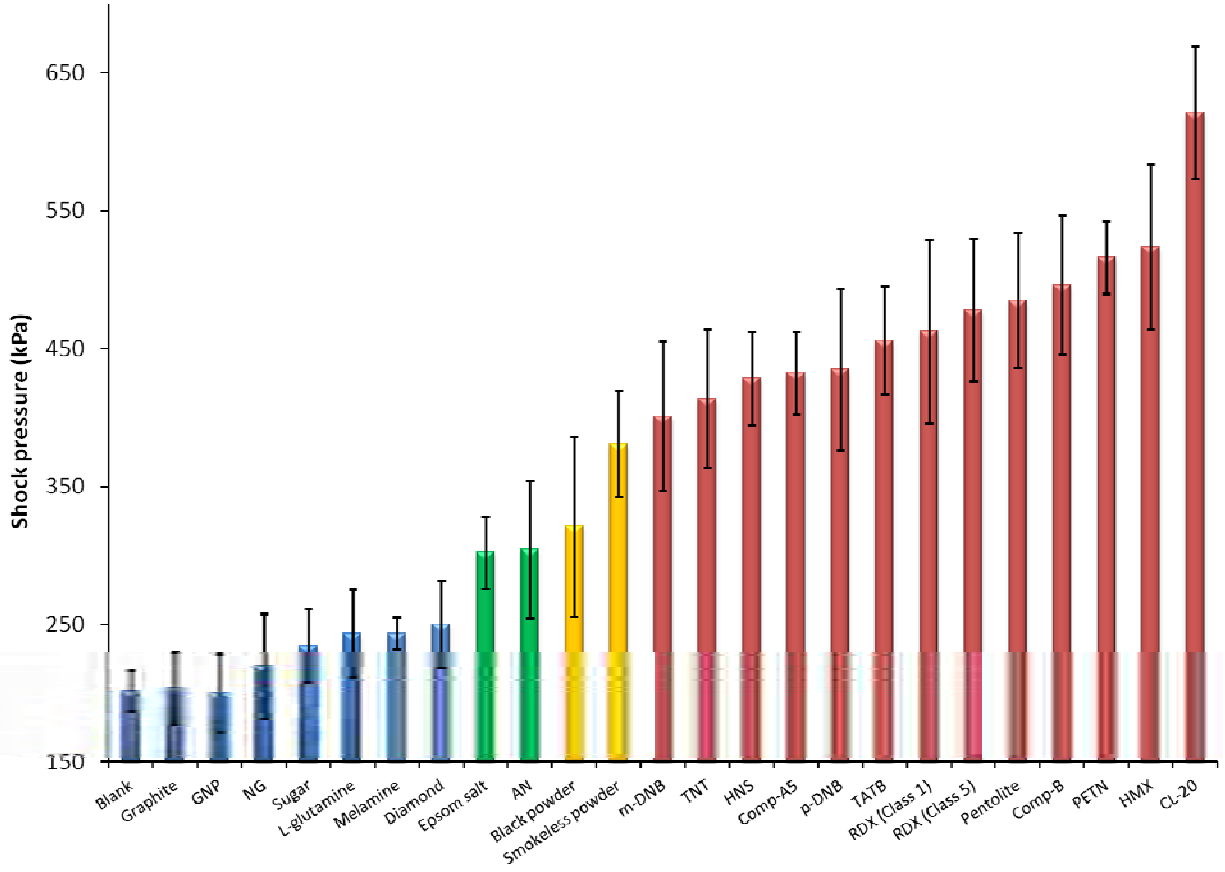

Figure 26. Laser-induced shock pressures for energetic and nonenergetic materials. Error bars represent 95% confidence intervals.

While the propellants (black powder, smokeless gun powder) also produced higher air shock pressures than the inert materials, the energetic materials produced the highest air shock pressures of all the materials investigated. CL-20, the most powerful conventional military explosive, produced the highest shock pressure. Although many of the confidence intervals between energetic materials overlap, the mean shock pressures can still be statistically significant at the 5% level with 25% overlap (*76*). For example, both TNT and Comp-B as well as HNS and PETN have statistically significant shock pressures at the 5% level (i.e., 95% probability that they are not the same). The complete results of a multiple comparison of means test are shown in figure 27. These results demonstrate that the laser-induced air shock waves can clearly be used to discriminate between energetic and nonenergetic materials.

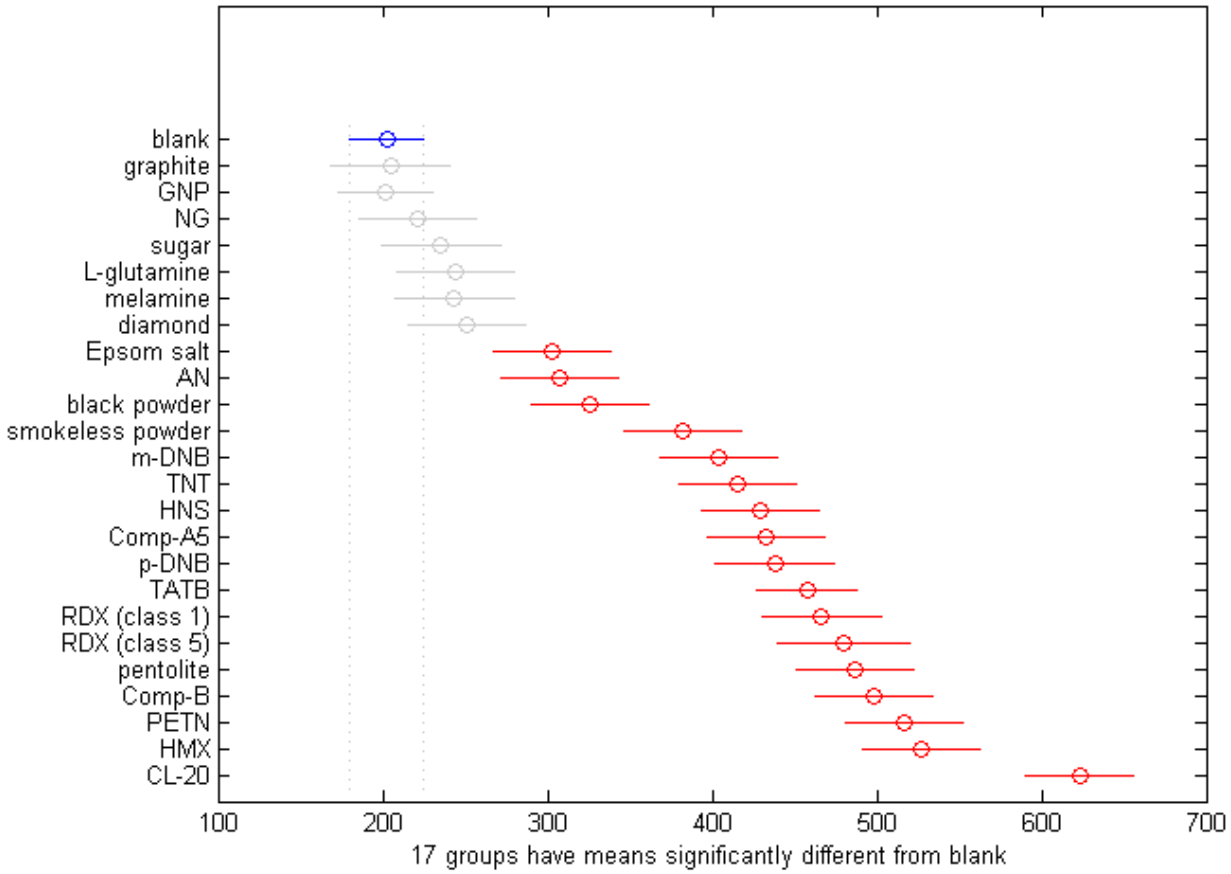

Figure 27. Results from a multiple comparison of means test at the 5% level demonstrating a significant difference in laser-induced shock pressures for nonenergetic and energetic materials.

The relationship between the air shock velocity and the properties of the explosives was also investigated. Table 3 lists the calculated properties of different explosives using the CHEETAH 6.0 code (*77*). Calculated parameters include the theoretical maximum density (TMD), the heat of combustion, and the detonation-related parameters, including heat of detonation, detonation velocity, and detonation pressure. While it is common to calculate the physical properties of the blast wave resulting from a theoretical chemical analysis of the explosive and its expected detonation products, there are several reasons why the calculated values may differ from the observed properties (*61*). For example, inefficiencies in the detonation process (e.g., a fraction of energy may be released in the form of radiation) may decrease the observed values, and additional energy released from the chemical reactions of the detonation products in atmospheric oxygen can increase the observed values. Table 4 lists the measured detonation velocities (corrected for the TMD) from large-scale testing of common explosives.

Table 3. Calculated explosive properties using CHEETAH 6.0 (*77*).

	Molecular Structure	TMD (g/cm^3)	Heat of combustion (kJ/g)	Heat of detonation (kJ/g)	Detonation velocity (km/s)	Detonation pressure (GPa)
m-DNB	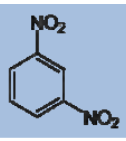	1.575	16.785	3.8186	6.589	15.609
p-DNB	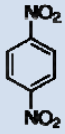	1.625	16.714	3.8305	6.78	16.69
TNT	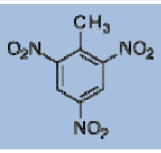	1.654	14.529	4.2297	7.179	20.053
HNS	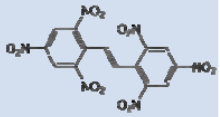	1.750	14.039	4.3999	7.493	23.082
Pentolite	50% PETN, 50% TNT	1.714	11.063	4.8563	7.606	25.063
Comp-B	60% RDX, 40% TNT	1.748	11.16	5.0889	8.004	27.007
TATB	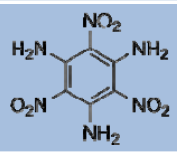	1.937	11.432	4.1868	8.451	30.177
PETN	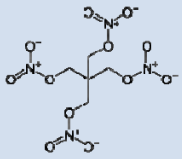	1.778	7.5977	5.9267	8.555	31.116
RDX	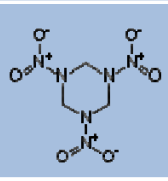	1.816	8.9138	5.7312	8.858	33.419
HMX	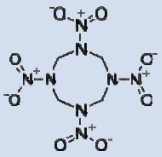	1.905	8.8519	5.7651	9.243	37.159
CL-20	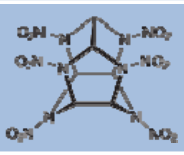	2.044	7.9424	6.1644	9.957	47.35

Table 4. Experimental detonation velocities for common explosives.

	Density (g/cm^3)	Detonation velocity (km/s)	Corrected detonation velocity (km/s)	Reference
m-DNB	1.47	6.1	6.4	(*78*)
TNT	1.6	6.7	6.88	(*46*)
TNT	1.630	6.93	7.00	(*79*)
TNT	1.550	6.85	7.16	(*80*)
TNT	1.6	6.90	7.06	(*78*)
HNS	1.70	7.00	7.00	(*80*)
HNS	1.600	6.80	7.25	(*79*)
TATB	1.80	7.35	7.76	(*78*)
TATB	1.88	7.76	7.93	(*79*)
Pentolite	1.700	7.53	7.57	(*79*)
Pentolite	1.65	7.40	7.59	(*78*)
Comp-B	1.715	7.89	7.99	(*46*)
Comp-B	1.65	7.80	8.09	(*78*)
PETN	1.7	8.40	8.63	(*78*)
PETN	1.77	8.26	8.28	(*79*)
PETN	1.60	7.92	8.45	(*78*)
RDX	1.6	8.13	8.78	(*46*)
RDX	1.767	8.70	8.85	(*79*)
RDX	1.70	8.44	8.79	(*80*)
RDX	1.76	8.75	8.92	(*78*)
HMX	1.9	9.10	9.12	(*78*)
HMX	1.890	9.11	9.16	(*79*)
CL-20	1.98	9.38	9.57	(*81*)

Figure 28 shows the correlation between the laser-induced air shock velocity and the calculated heats of combustion. Linear regression was used to determine the best fit for the weighted data (solid black line). Error bars correspond to 95% confidence intervals, the blue dotted lines correspond to confidence bands for the fit (region within which the measured data are expected to fall with 95% confidence), and the red dashed lines correspond to prediction bands (region within which random samples from the model plus random errors are expected to fall). The fit coefficients and linear fit coefficient r (Pearson's r) are also shown. The data show a weak negative correlation between the laser-induced air shock velocity and the calculated heat of combustion. For comparison, the correlation between the measured detonation velocities (from table 4) and the calculated heats of combustion (table 3) is shown in figure 29. The measured detonation velocities (averaged for the available experimental measurements) also show a negative correlation with the calculated heat of combustion.

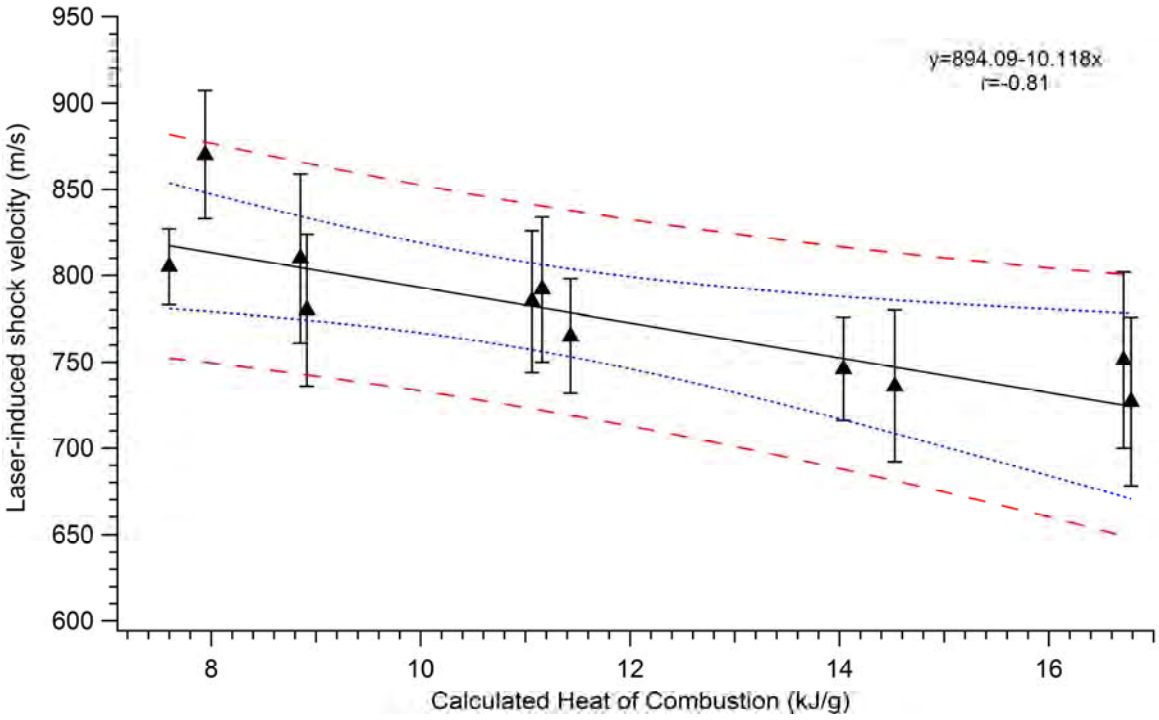

Figure 28. Correlation between the laser-induced air shock velocity and the calculated heat of combustion for energetic materials.

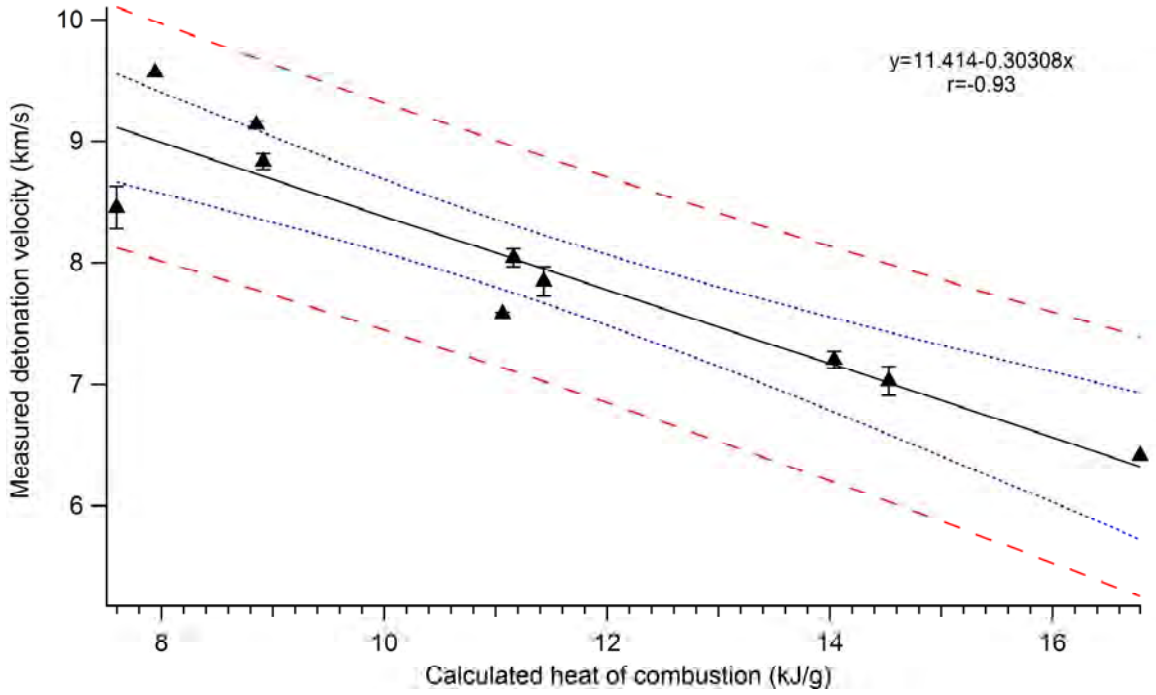

Figure 29. Correlation between the measured detonation velocity and the calculated heat of combustion for energetic materials.

The heat of combustion is a measure of the energy released when the explosive (or other material) burns in the presence of excess oxygen (resulting in complete oxidation). The heat of detonation (or energy of detonation), on the other hand, is the energy released by the detonation of the explosive material in an inert atmosphere. The further oxidation of detonation products in air can lead to additional energy release subsequent to the initial detonation, e.g., the phenomenon known as “after-burning” in TNT explosions (*82*). Thus, the heat of detonation may be less than the total energy released during the complete combustion of an explosive, depending on the oxygen balance of the explosive. The negative correlation between the detonation velocity (or performance) of an explosive and the heat of combustion thus suggests that the more powerful explosives produce more highly oxidized products during detonation.

Although more energy is released through the subsequent combustion reactions of the less powerful explosives, those reactions occur on a much slower timescale, which is typically not ideal for high explosives applications (but may be for propellants where extended thrust is required). Figure 30 shows the correlation between the laser-induced air shock velocity and the calculated energy of detonation. In this case, the expected positive correlation is observed. This suggests that the atomization and subsequent recombination of atoms from the energetic material that result in the increased air shock velocity occur before atmospheric oxygen (and nitrogen) is incorporated in the laser-induced plasma. Previous observations that the molecular cyano radical (CN) is formed from the recombination of ablated carbon and atmospheric nitrogen after approximately 2–3 μs (*15*) substantiate this conclusion since the air shock wave is formed on a significantly shorter timescale.

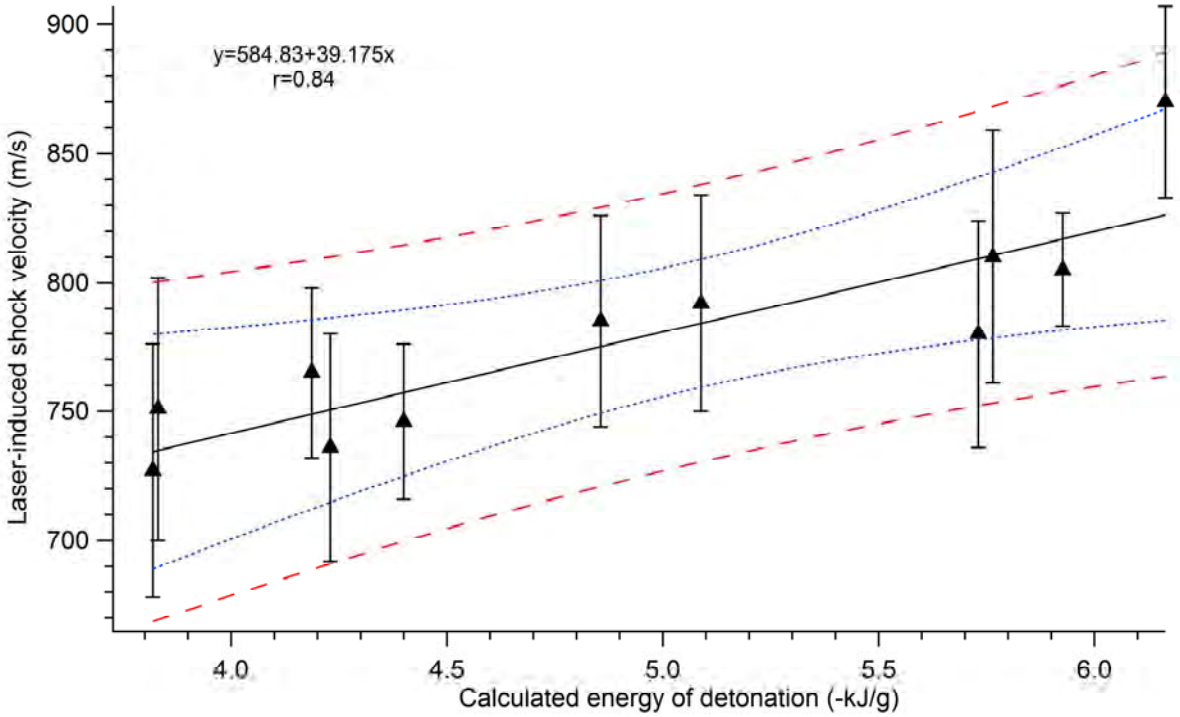

Figure 30. Correlation between the laser-induced air shock velocity and the calculated energy of detonation for energetic materials.

Figure 31 shows the correlation between the laser-induced air shock velocity and the calculated detonation velocity. A relatively strong positive correlation was observed. Using measured detonation velocities resulted in a slightly improved fit (figure 32); unfortunately, measured detonation velocities were not available for all of the energetic materials investigated here. While the experimental detonation velocities have been corrected for the theoretical maximum density, the density of the prepared explosive residue samples is not controlled. Preparation of explosive samples with precise densities generally requires formulation to enable pressing the sample into pellets or inkjet printing, which can be challenging for certain materials because of the strict solvent requirements; for the laboratory-scale shock measurements it is not desirable to limit the types of samples that can be studied.

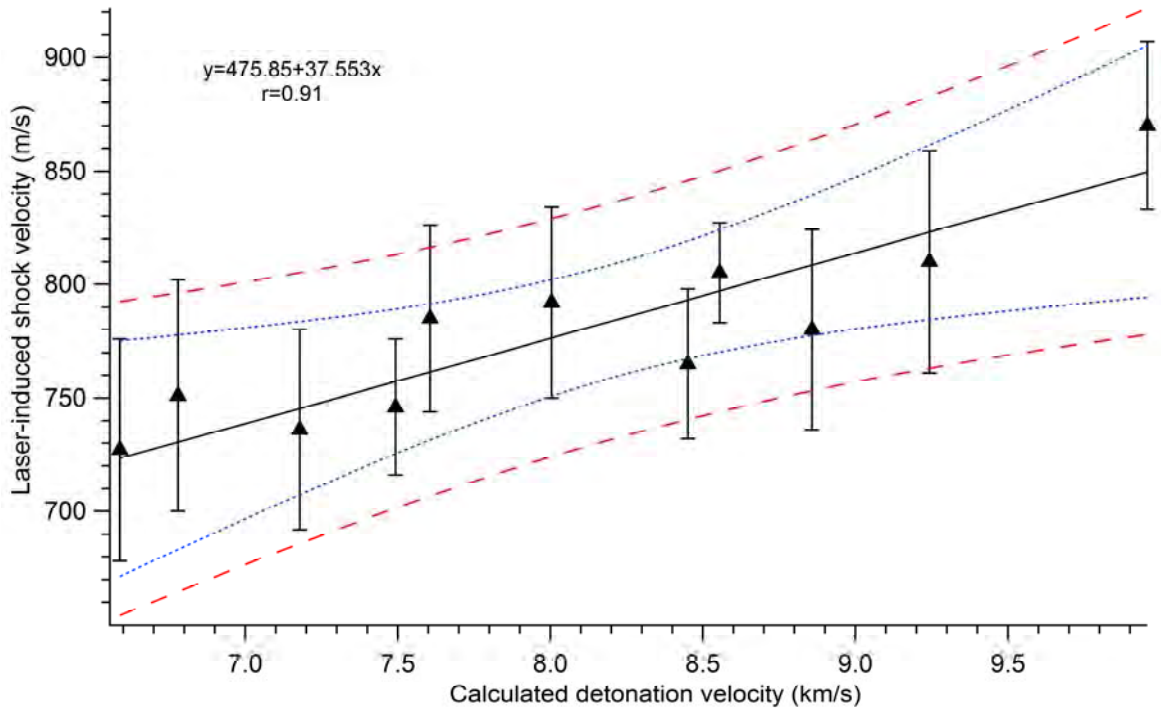

Figure 31. Correlation between the laser-induced air shock velocity and the calculated detonation velocity for energetic materials.

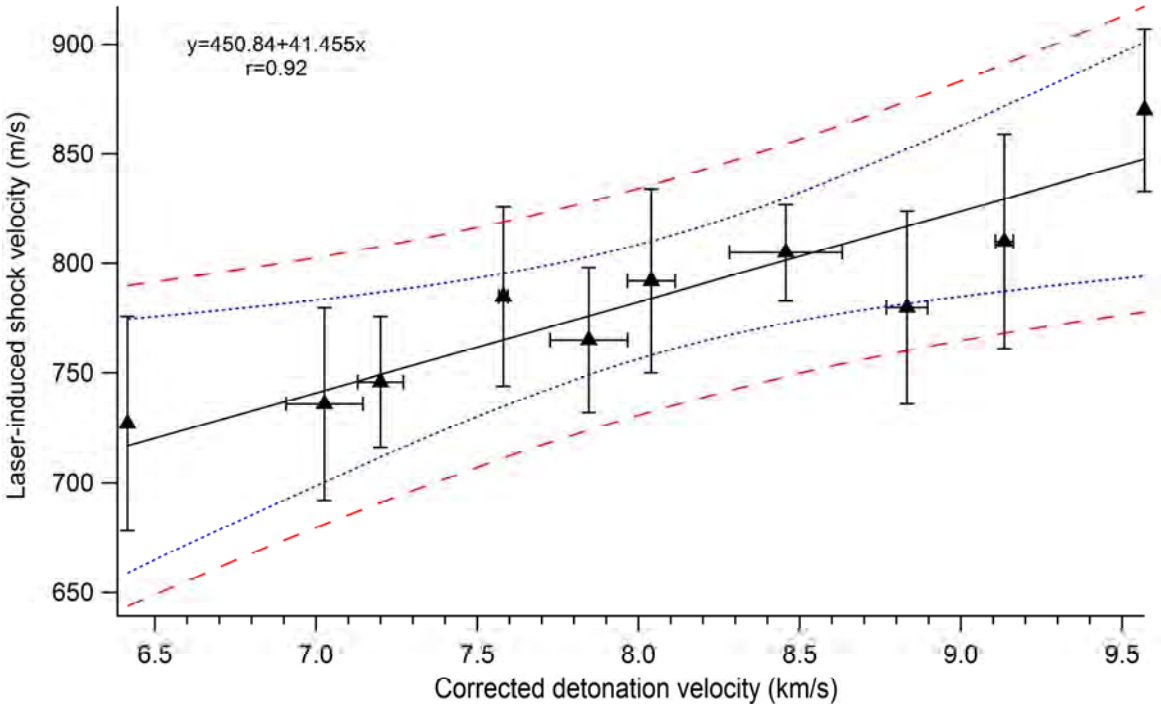

Figure 32. Correlation between the laser-induced air shock velocity and the measured detonation velocity for energetic materials.

Based on the correlation observed in figure 32, the estimated detonation velocities for those explosives with measured detonation velocities (see table 4 for references) are given in table 5. No corrections were made for the laser-shocked sample density. The average absolute error in the estimated detonation velocities was 4.1%, and the standard deviation was 2.8%. The most significant error is the estimated detonation velocity for RDX; some of the difference between the estimated and measured values could be attributable to the class of RDX used in the detonative testing or the conditions of the testing (neither of which was specified in the reference tables).

Table 5. Estimated detonation velocities for common explosives based on laser-induced air shock velocities.

	Measured detonation velocity (km/s)	Estimated detonation velocity (km/s)	% Difference
m-DNB	6.42	6.66	3.8%
TNT	7.03	6.88	-2.1%
HNS	7.20	7.13	-1.0%
TATB	7.85	7.59	-3.3%
RDX	8.83	7.95	-10.0%
Pentolite	7.58	8.06	6.3%
Comp-B	8.04	8.24	2.5%
HMX	9.14	8.67	-5.1%
PETN	8.46	8.55	1.1%
CL-20	9.57	10.11	5.6%

Finally, the correlation between the laser-induced air shock velocity and the calculated detonation pressure is shown in figure 33. A relatively strong positive correlation was obtained, so that this method could also be used to estimate detonation pressures. A comparison between the laser-induced shock pressure and the calculated detonation pressure produced similar results (not shown), although the r value for the fit was slightly worse ($r = 0.93$).

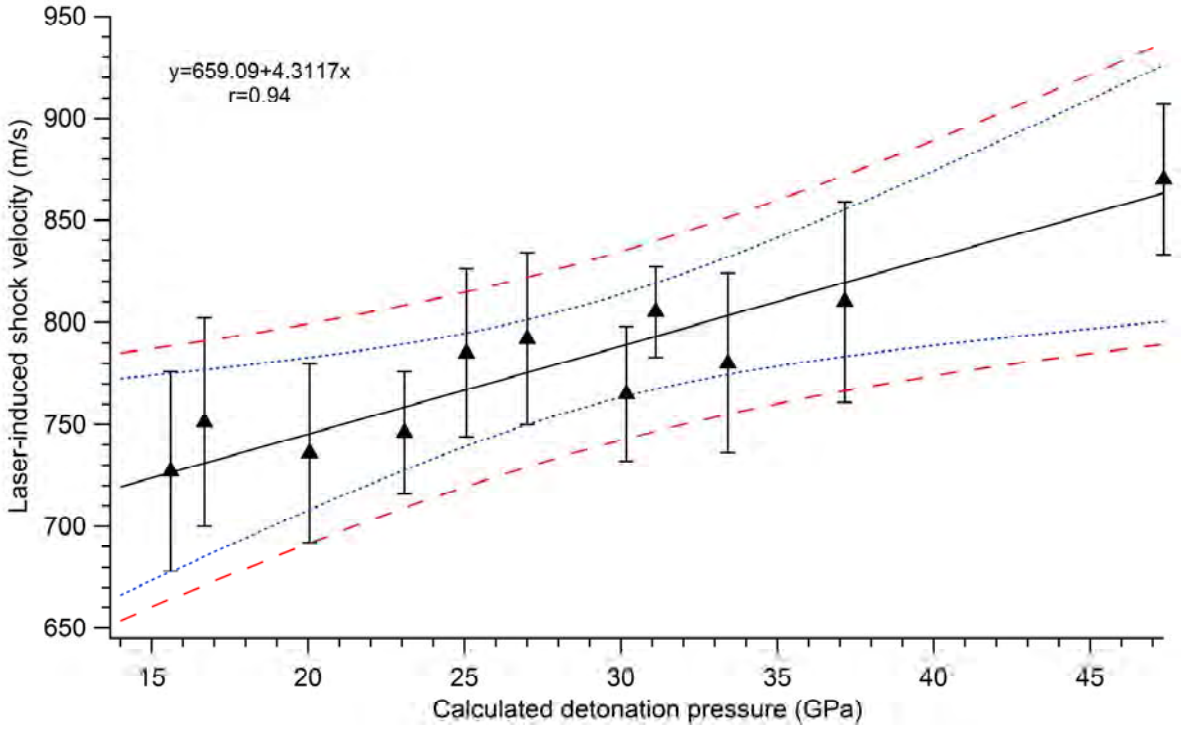

Figure 33. Correlation between the laser-induced air shock velocity and the calculated detonation pressure for energetic materials.

4.4 Determination of Explosive Performance for Test Materials

In order to demonstrate the utility of this method for the estimation of detonation performance using only milligram quantities of materials (where larger quantities were not available for full-scale detonation testing), several classes of new explosives or explosive formulations were studied. Three different high-nitrogen explosives under consideration for military use were tested, including 5,5′-hydrazinebistetrazole (HBT) (*83*), 5,5′-bis(1*H*-tetrazolyl)amine (H_2bta) (*84*), and triaminoguanidinium-1-methyl-5-nitrominotetrazolate (TAG-MNT) (*85*). The laser-induced plasma chemistry of these and other high-nitrogen compounds has been previously studied (*12*). Like the conventional energetic materials, the plasma emission from the high-nitrogen compounds is decreased compared to nonenergetic materials (figure 23 M–O).

The calculated values for detonation velocity and pressure from CHEETAH (*77*) and EXPLO5 software (*86*) (values provided in papers from the Klapötke group [*83–85*]) were compared with the values estimated using the laser-induced shock experiment (table 6). While the laser-induced shock experiments agreed with the calculated detonation parameters for the H_2bta within 10%, they suggested lower explosive performance than expected for HBT and higher than expected performance for TAG-MNT. Without experimental detonation data it is difficult to speculate on the reason for these discrepancies, since the accuracy of the models for these types of high-nitrogen materials is not known.

A number of potential new energetic materials based on mechanical rather than chemical energy release have also been tested. The experimental results for these samples are also listed in table 6 (samples 1–5). Based on these (and other confirmatory) results, samples 3–5 were selected for further testing. Potential new explosive formulations of conventional energetic materials have also been studied with this method. This technique is expected to be widely applicable to a variety of materials; it will be particularly useful as a prescreening tool prior to larger-scale testing, especially when only small quantities (milligrams) are available for initial testing.

Table 6. Estimated detonation velocities for potential new energetic materials based on laser-induced air shock velocities.

	Calc. det. vel. – CHEETAH (km/s)	Calc. det. vel. – EXPLO5 (km/s)	Est. det. vel. (km/s)	Calc. det. pressure – CHEETAH (GPa)	Calc. det. pressure – EXPLO5 (GPa)	Est. det. pressure (GPa)
BHT	9.211	8.523	7.11	31.077	27.7	20.1
H_2bta	9.6	9.12	9.04	35.677	34.3	38.6
TAG-MNT	8.634	8.770	10.4	26.004	27.3	51.5
Sample 1	N/A	N/A	4.64	N/A	N/A	---
Sample 2	N/A	N/A	6.45	N/A	N/A	13.7
Sample 3	N/A	N/A	7.11	N/A	N/A	20.0
Sample 4	N/A	N/A	8.23	N/A	N/A	30.8
Sample 5	N/A	N/A	11.4	N/A	N/A	61.7

5. Conclusions

Although previous laser-induced shock studies on metal targets found no evidence for chemical reactions behind the shock front—and thus disputed the link between the laser-induced blast wave and a detonation wave (*21*, *39*)—our results indicate that for nonmetal samples which undergo exothermic reactions upon decomposition, chemical reactions in the vapor plume behind the shock front affect the shock front velocity. Thus, under certain experimental conditions (e.g., laser fluence) with chemically reactive materials, the laser-supported blast wave is similar to a detonation wave. One major difference is that the shock front travels first through the plasma plume containing evaporated material and then through the ambient air, as opposed to a true detonation wave that travels through the solid energetic material. While previous experiments measured the position of the shock wave up to several microseconds using a charge-coupled device camera to capture a single frame from each laser ablation event, this experiment measured

the shock wave position up to 200 μs using more than 15 frames for each event. In addition, the laser pulse energy for this experiment (900 mJ) was considerably higher than typical pulse energies used for laser-induced shock experiments (<200 mJ).

Unlike previous laser-induced shock studies on nonenergetic materials, the thermal energy in the energetic material vapor plume was caused by both the energy transferred from the laser and the subsequent exothermic chemical reactions of the ablated species. The Sedov-Taylor model was not applicable for any of the samples studied here because of the distance from the target (and because of the chemical reactions in the plasma). While the drag model worked well for inert materials, the Dewey fit worked best for the energetic materials. No single model could be found to fit both energetic and nonenergetic materials.

Based on the initial promising results, a new laboratory-scale method for predicting explosive performance (e.g., detonation velocity and pressure) using milligram quantities of material is currently being developed. Preliminary results on a suite of conventional energetic materials, including RDX, TNT, HMX, PETN, HNS, TATB, CL-20, composition-B, composition-A5, and Pentolite, show a strong linear correlation between the laser-induced air shock velocity and the measured performance from full-scale detonation testing. Estimated detonation velocities based on the laser-induced air shock velocities differ from values obtained through large-scale detonative testing by less than 10%. This method is a potential screening tool for the development of new energetic materials and formulations prior to large-scale testing. This method would be particularly useful in several situations: when candidate materials are only available in limited quantities; for energetic materials with a larger critical diameter, where small-scale detonative testing (*87*) is not possible; or for materials that require nonconventional means to induce detonation.

Potential sources of error in the laser-induced shock measurements include differences in the absorption coefficients of the energetic materials, fluctuations in laser energy, jitter in the camera triggering, measurement of the shock positions, differences in the amount of material ablated from shot to shot, and unusually high luminosity in the first few camera frames that obscures the shock front. Ideally, a camera with a faster frame rate should be used to better measure the shock position at earlier times. Planned improvements to the current experiment include exploring alternative sample preparation methods (although shot-to-shot fluctuations are inherent to laser ablation, and it has been suggested that the relationship between the shock wave energy and the amount of material ablated is lost anyway because of the complexity of the laser-material interaction [*42*]), decreasing the confidence intervals by increasing the number of laser shots per material, and automating the data analysis process. Additional energetic materials will also be tested with this method.

6. References

1. Brech, F.; Cross, L. Optical Microemission Stimulated by a Ruby Laser. *Appl. Spectrosc.* **1962,** *16,* 59.
2. Bogaerts, A.; Chen, Z.; Gijbels, R.; Vertes, A. Laser Ablation for Analytical Sampling: What Can We Learn From Modeling? *Spectrochim. Acta, Part B* **2003,** *58* (11), 1867–1893.
3. von Allmen, M.; Blatter, A. *Laser-Beam Interactions With Materials: Physical Principles and Applications,* 2nd ed.; Springer-Verlag: Berlin Heidelberg, 2002.
4. Gagliano, F. P.; Paek, U. C. Observation of Laser-Induced Explosion of Solid Materials and Correlation with Theory. *Appl. Opt.* **1974,** *13* (2), 274–279.
5. Brailovsky, A. B.; Gaponov, S. V.; Luchin, V. I. Mechanisms of Melt Droplets and Solid-Particle Ejection From a Target Surface by Pulsed Laser Action. *Appl. Phys. A* **1995,** *61* (1), 81–86.
6. Miotello, A.; Kelly, R. Laser-Induced Phase Explosion: New Physical Problems When a Condensed Phase Approaches the Thermodynamic Critical Temperature. *Appl. Phys. A* **1999,** *69* (0), S67–S73.
7. Yoo, J. H.; Jeong, S. H.; Greif, R.; Russo, R. E. Explosive Change in Crater Properties During High Power Nanosecond Laser Ablation of Silicon. *J. Appl. Phys.* **2000,** *88* (3), 1638–1649.
8. Wen, S.-B.; Mao, X.; Greif, R.; Russo, R. E. Expansion of the Laser Ablation Vapor Plume Into a Background Gas. I. Analysis. *J. Appl. Phys.* **2007,** *101* (2), 023114.
9. Harilal, S. S.; Bindhu, C. V.; Tillack, M. S.; Najmabadi, F.; Gaeris, A. C. Internal Structure and Expansion Dynamics of Laser Ablation Plumes into Ambient Gases. *J. Appl. Phys.* **2003,** *93* (5), 2380–2388.
10. Cremers, D. A.; Radziemski, L. J. *Handbook of Laser-Induced Breakdown Spectroscopy,* 2nd ed.; John Wiley & Sons, Ltd.: Singapore, 2013.
11. Gottfried, J. L.; De Lucia, F. C., Jr.; Munson, C. A.; Miziolek, A. W. Laser-Induced Breakdown Spectroscopy for Detection of Explosives Residues: A Review of Recent Advances, Challenges, and Future Prospects. *Anal. Bioanal. Chem.* **2009,** *395* (2), 283–300.
12. De Lucia, F. C., Jr.; Gottfried, J. L. Characterization of a Series of Nitrogen-Rich Molecules Using Laser-Induced Breakdown Spectroscopy. *Propellants, Explos., Pyrotech.* **2010,** *35* (3), 268–277.

13. De Lucia, F. C., Jr.; Gottfried, J. L. Classification of Explosive Residues on Organic Substrates Using Laser Induced Breakdown Spectroscopy *Appl. Opt.* **2012,** *51* (7), B83–B92.

14. Singh, R. Transient Plasma Shielding Effects During Pulsed Laser Ablation of Materials. *J. Electron. Mater.* **1996,** *25* (1), 125–129.

15. Gottfried, J. L. Laser-Induced Plasma Chemistry of the Explosive RDX With Various Metallic Nanoparticles. *Appl. Opt.* **2012,** *51* (7), B13–B21.

16. Gottfried, J. L.; Densmore, J. M. Laser-Induced Breakdown Spectroscopy of Reactive Materials Doped With Carbon Nanoparticles. *JANNAF J. Prop. Energ.* **2013,** *6* (1), 23–35.

17. Radziemski, L. J.; Cremers, D. A., Eds. *Modeling of Post-Breakdown Phenomena: Laser-Induced Plasma and Applications;* Marcel Dekker: New York, 1989.

18. Taylor, G. The Formation of a Blast Wave by a Very Intense Explosion I. Theoretical Discussion. *Proc. R. Soc. A* **1950,** *201* (1065), 159–174.

19. Grun, J.; Stamper, J.; Manka, C.; Resnick, J.; Burris, R.; Ripin, B. H. Observation of High-Pressure Blast-Wave Decursors. *Appl. Phys. Lett.* **1991,** *59* (2), 246–248.

20. Aden, M.; Kreutz, E. W.; Schlüter, H.; Wissenbach, K. The Applicability of the Sedov - Taylor Scaling During Material Removal of Metals and Oxide Layers With Pulsed CO_2 and Excimer Laser Radiation. *J. Appl. Phys. D* **1997,** *30* (6), 980.

21. Callies, G.; Berger, P.; Hugel, H. Time-Resolved Observation of Gas-Dynamic Discontinuities Arising During Excimer Laser Ablation and Their Interpretation. *J. Phys. D* **1995,** *28* (4), 794.

22. Sedov, L. I. *Similarity and Dimensional Methods in Mechanics;* Cleaver Hume: London, 1959.

23. Zeng, X.; Mao, X. L.; Greif, R.; Russo, R. E. Experimental Investigation of Ablation Efficiency and Plasma Expansion During Femtosecond and Nanosecond Laser Ablation of Silicon. *Appl. Phys. A* **2005,** *80* (2), 237–241.

24. Maher, W. E.; Hall, R. B. An Interferometric Investigation of Laser-Supported Absorption Waves. *J. Appl. Phys.* **1975,** *46* (2), 761–772.

25. Ramsden, S. A.; Savic, P. A Radiative Detonation Model for the Development of a Laser-Induced Spark in Air. *Nature* **1964,** *203* (4951), 1217–1219.

26. Raizer, Y. P. Heating of a Gas by a Powerful Light Pulse. *Sov. Phys.-JETP* **1965,** *21,* 1009–1017.

27. Maher, W. E.; Hall, R. B.; Johnson, R. R. Experimental Study of Igition and Propagation of Laser-Supported Detonation Waves. *J. Appl. Phys.* **1974,** *45* (5), 2138–2145.

28. Ushio, M.; Komurasaki, K.; Kawamura, K.; Arakawa, Y. Effect of Laser Supported Detonation Wave Confinement on Termination Conditions. *Shock Waves* **2008,** *18* (1), 35–39.

29. Kim, C.-H.; Ardian, G. B.; Yoh, J. J. Surface Chemical Reaction of Laser Ablated Aluminum Sample for Detonation Initiation. *J. Appl. Phys.* **2011,** *109* (9), 093510.

30. Geohegan, D. B. Fast Intensified-CCD Photography of YBa2Cu3O7−x Laser Ablation in Vacuum and Ambient Oxygen. *Appl. Phys. Lett.* **1992,** *60* (22), 2732–2734.

31. Kushwaha, A.; Thareja, R. K. Dynamics of Laser-Ablated Carbon Plasma: Formation of C2 and CN. *Appl. Opt.* **2008,** *47* (31), G65–G71.

32. Gonzalo, J.; Afonso, C. N.; Madariaga, I. Expansion Dynamics of the Plasma Produced by Laser Ablation of $BaTiO_3$ in a Gas Environment. *J. Appl. Phys.* **1997,** *81* (2), 951–955.

33. Dyer, P. E.; Sidhu, J. Spectroscopic and Fast Photographic Studies of Excimer Laser Polymer Ablation. *J. Appl. Phys.* **1988,** *64* (9), 4657–4663.

34. Kokai, F.; Takahashi, K.; Shimizu, K.; Yudasaka, M.; Iijima, S. Shadowgraphic and Emission Imaging Spectroscopic Studies of the Laser Ablation Of Graphite in an Ar Gas Atmosphere. *Appl Phys A* **1999,** *69* (1), S223–S227.

35. Salleo, A.; Genin, F. Y.; Feit, M. D.; Rubenchik, A. M.; Sands, T.; Mao, S. S.; Russo, R. E. Energy Deposition at Front and Rear Surfaces During Picosecond Laser Interaction With Fused Silica. *Appl. Phys. Lett.* **2001,** *78* (19), 2840–2842.

36. Zeng, X.; Mao, X.; Wen, S.-B.; Greif, R.; Russo, R. E. Energy Deposition and Shock Wave Propagation During Pulsed Laser Ablation in Fused Silica Cavities. *J. Phys. D* **2004,** *37* (7), 1132.

37. Zheng, Z.-Y.; Zhang, Y.; Zhao, C.-C.; Hao, H.-Y.; Lu, X.; Li, Y.-T.; Zhang, J. Ablation Pressure of the Shock Wave Generated by Laser Interaction With Solid Targets. *Optelec. Lett.* **2007,** *3* (5), 394–396.

38. Zhang, N.; Zhu, X.; Yang, J.; Wang, X.; Wang, M. Time-Resolved Shadowgraphs of Material Ejection in Intense Femtosecond Laser Ablation of Aluminum. *Phys. Rev. Lett.* **2007,** *99* (16), 167602.

39. Yoh, J. J.; Lee, H.; Choi, J.; Lee, K.-C.; Kim, K.-H. Ablation-Induced Explosion of Metal Using a High-Power Nd:YAG Laser. *J. Appl. Phys.* **2008,** *103* (4), 043511-6.

40. Gravel, J.-F. Y.; Boudreau, D. Study by Focused Shadowgraphy of the Effect of Laser Irradiance on Laser-Induced Plasma Formation and Ablation Rate in Various Gases. *Spectrochim. Acta, Part B* **2009,** *64* (1), 56–66.

41. Porneala, C.; Willis, D. A. Time-Resolved Dynamics of Nanosecond Laser-Induced Phase Explosion. *J. Phys. D-Appl. Phys.* **2009,** *42* (15), 155503.

42. Schmitz, T. A.; Koch, J.; Günther, D.; Zenobi, R. Early Plume and Shock Wave Dynamics in Atmospheric-Pressure Ultraviolet-Laser Ablation of Different Matrix-Assisted Laser Ablation Matrices. *J. Appl. Phys.* **2011,** *109* (12), 123106.

43. Harilal, S. S.; Miloshevsky, G. V.; Diwakar, P. K.; LaHaye, N. L.; Hassanein, A. Experimental and Computational Study of Complex Shockwave Dynamics in Laser Ablation Plumes in Argon Atmosphere. *Phys. Plasmas* **2012,** *19* (8), 083504–11.

44. Sanginés, R.; Sobral, H. Time Resolved Study of the Emission Enhancement Mechanisms in Orthogonal Double-Pulse Laser-Induced Breakdown Spectroscopy. *Spectrochim. Acta, Part B* **2013,** *88*, 150–155.

45. Roy, S.; Jiang, N.; Stauffer, H. U.; Schmidt, J. B.; Kulatilaka, W. D.; Meyer, T. R.; Bunker, C. E.; Gord, J. R. Spatially and Temporally Resolved Temperature and Shock-Speed Measurements Behind a Laser-Induced Blast Wave of Energetic Nanoparticles. *J. Appl. Phys.* **2013,** *113* (18), 184310.

46. Cooper, P. *Explosives Engineering*; Wiley-VCH: New York, 1996.

47. Deal, W. E. Shock Hugoniot of Air. *J. Appl. Phys.* **1957,** *28* (7), 782–784.

48. Kim, I. H.; Hong, S. H.; Jhung, K. S.; Oh, K. -H.; Yoon, Y. K. Relationship Among Shock-Wave Velocity, Particle Velocity, and Adiabatic Exponent for Dry Air. *J. Appl. Phys.* **1991,** *70* (2), 1048–1050.

49. Gottfried, J. L. *Laser-Induced Deflagration of Nanodiamond-Enhanced RDX*; ARL-TR-5519; U.S. Army Research Laboratory: Aberdeen Proving Ground, MD, 2011.

50. Gottfried, J. L. *Laser-Shocked Nanodiamonds*; ARL-TR-5611; U.S. Army Research Laboratory: Aberdeen Proving Ground, MD, 2011.

51. Gottfried, J. L. *Laser-Induced Deflagration of Nanodiamond-Enhanced TNT*; ARL-TR-6321; U.S. Army Research Laboratory: Aberdeen Proving Ground, MD, 2013.

52. Gottfried, J. L. *Optimization of Nanodiamond Concentration in Energetic Material Mixtures*; ARL-TR-6718; U.S. Army Research Laboratory: Aberdeen Proving Ground, MD, 2013.

53. Hall, R. B. Laser Production of Blast Waves in Low Pressure Gases. *J. Appl. Phys.* **1969,** *40* (4), 1941–1945.

54. Wen, S.-B.; Mao, X.; Greif, R.; Russo, R. E. Laser Ablation Induced Vapor Plume Expansion Into a Background Gas. II. Experimental Analysis. *J. Appl. Phys.* **2007**, *101* (2), 023115–14.

55. Amoruso, S.; Schou, J.; Lunney, J. Influence of the Atomic Mass of the Background Gas on Laser Ablation Plume Propagation. *Appl. Phys. A* **2008,** *92* (4), 907–911.

56. Thiyagarajan, M.; Williamson, K.; Kandi, A. R. Experimental Investigation of 1064-nm IR Laser-Induced Air Plasma Using Optical Laser Shadowgraphy Diagnostics. *IEEE Trans. Plasma Sci.* **2012,** *40* (10), 2491–2500.

57. Ben-Eliahu, Y.; Haas, Y.; Welner, S. Laser Initiation of the Decomposition of Energetic Polymers: Shock Wave Formation. *J. Phys. Chem.* **1995,** *99* (16), 6010–6018.

58. Haas, Y.; Ben-Eliahu, Y.; Welner, S. Pulsed Laser Induced Decomposition of Energetic Polymers: Comparison of Ultraviolet (355 nm) and Infrared (9.3 μm) Initiation. *Propellants, Explos., Pyrotech.* **1996,** *21* (5), 258–265.

59. Belau, L.; Ben-Eliahu, Y.; Hecht, I.; Kop, G.; Haas, Y.; Welner, S. Laser-Induced Dissociation of an Energetic Polymer: A Spectroscopic Study of the Gaseous Products. *J. Phys. Chem. B* **2000,** *104* (44), 10154–10161.

60. Hauer, M.; Funk, D. J.; Lippert, T.; Wokaun, A. Time Resolved Study of the Laser Ablation Induced Shockwave. *Thin Solid Films* **2004,** 453–454, 584.

61. Kleine, H.; Dewey, J. M.; Ohashi, K.; Mizukaki, T.; Takayama, K. Studies of the TNT Equivalence of Silver Azide Charges. *Shock Waves* **2003,** *13* (2), 123–138.

62. Settles, G. S. Experimental Fluid Mechanics. In *Schlieren and Shadowgraph Techniques*; Adrian, R. J., et al., Eds.; Springer-Verlag: New York, 2001.

63. Brode, H. L. *The Blast Wave in Air Resulting From a High Temperature, High Pressure Sphere of Air*; RM-1825-AEC; U.S. Atomic Energy Commission: Santa Monica, CA, 1956.

64. Freiwald, D. A.; Axford, R. A. Approximate Spherical Blast Theory Including Source Mass. *J. Appl. Phys.* **1975,** *46* (3), 1171–1174.

65. Jeong, S. H.; Greif, R.; Russo, R. E. Propagation of the Shock Wave Generated From Excimer Laser Heating of Aluminum Targets in Comparison With Ideal Blast Wave Theory. *Appl. Surf. Sci.* **1998**, 127–129 (0), 1029–1034.

66. Jeong, S. H.; Greif, R.; Russo, R. E. Shock Wave and Material Vapour Plume Propagation During Excimer Laser Ablation of Aluminium Samples. *J. Phys. D* **1999,** *32* (19), 2578–2585.

67. Bennett, L. S.; Lippert, T.; Furutani, H.; Fukumura, H.; Masuhara, H. Laser Induced Microexplosions of a Photosensitive Polymer. *Appl. Phys. A* **1996,** *63* (4), 327–332.

68. Srinivasan, R.; Braren, B.; Casey, K. G.; Yeh, M. Ultrafast Imaging of Ultraviolet Laser Ablation and Etching of Polymethylmethacrylate. *Appl. Phys. Lett.* **1989,** *55* (26), 2790–2791.

69. Hutchens, G. J. Approximate Near-Field Blast Theory: A Generalized Approach. *J. Appl. Phys.* **2000,** *88* (6), 3654–3658.

70. Dewey, J. M. The Properties of a Blast Wave Obtained From an Analysis of the Particle Trajectories. *Proc. Roy. Soc. A* **1971,** *324* (1558), 275–299.

71. Shimizu, T. An Example of Negative Explosives: Magnesium Sulfate/Magnesium Mixture. *Proceedings of the 15th International Pyrotechnics Seminar*, Boulder, CO, 9–13 July, 1990.

72. Pearse, R. W. B.; Gaydon, A. G. *The Identification of Molecular Spectra*, 4th ed.; John Wiley & Sons, Inc: New York, 1976.

73. Sinditskii, V. P.; Egorshev, V. Y.; Levshenkov, A. I.; Serushkin, V. V. Ammonium Nitrate: Combustion Mechanism and the Role of Additives. *Propellants, Explos., Pyrotech.* **2005,** *30* (4), 269–280.

74. Gottfried, J. L.; De Lucia, F. C., Jr.; Munson, C. A.; Miziolek, A. W. Standoff Detection of Chemical and Biological Threats Using Laser-Induced Breakdown Spectroscopy. *Appl. Spectrosc.* **2008, 62** (4), 353–363.

75. Tsuyuki, K.; Miura, S.; Idris, N.; Kurniawan, K. H.; Lie, T. J.; Kagawa, K. Measurement of Concrete Strength Using the Emission Intensity Ratio Between Ca(II) 396.8 nm and Ca(I) 422.6 nm in a Nd:YAG Laser-Induced Plasma. *Appl. Spectrosc.* **2006,** *60* (1), 61–64.

76. Wolfe, R.; Hanley, J. If We're So Different, Why Do We Keep Overlapping? When 1 plus 1 Doesn't Make 2. *CMAJ* **2002,** *166* (1), 65–66.

77. Bastea, S.; Fried, L. E.; Glaesemann, K. R.; Howard, W. M.; Kuo, I.-F.W.; Souers, P. C.; Vitello, P. A. *CHEETAH 6.0*; Energetic Materials Center, Lawrence Livermore National Laboratory: Livermore, CA, 24 May 2010.

78. Meyer, R.; Köhler, J.; Homburg, A. *Explosives*, 6th ed.; Wiley-VCH: Weinheim, 2007.

79. Cooper, P. W.; Kurowski, S. R. *Introduction to the Technology of Explosives*; Wiley-VCH, Inc.: New York, 1996.

80. Akhavan, J. *The Chemistry of Explosives*, 2nd ed.; The Royal Society of Chemistry: Cambridge, UK, 2004.

81. Detonation Velocity and Lead Block Test. http://mihailru.freeservers.com/shopping_page .html (accessed 13 September 2013).

82. Dewey, J. M. The Air Velocity in Blast Waves from TNT Explosions. *Proc. Roy. Soc. A* **1964,** *279* (1378), 366–385.

83. Klapoetke, T. M.; Sabate, C. M. Bistetrazoles: Nitrogen-Rich, High-Performing, Insensitive Energetic Compounds. *Chem. Mater.* **2008,** *20* (11), 3629–3637.

84. Klapoetke, T. M.; Mayer, P.; Stierstorfer, J.; Weigand, J. J. Bistetrazolylamines-Synthesis and Characterization. *J. Mater. Chem.* **2008,** *18* (43), 5248–5258.

85. Klapötke, T. M.; Stierstorfer, J.; Wallek, A. U. Nitrogen-Rich Salts of 1-Methyl-5-nitriminotetrazolate: An Auspicious Class of Thermally Stable Energetic Materials. *Chem. Mater.* **2008,** *20* (13), 4519–4530.

86. Suceska, M. Computer Program for Calculation of Detonation Parameters. *Proceedings of the 32nd Int. Annual Conference of ICT*, Karlsruhe, Germany, 3–6 July 2001.

87. Biss, M. M. Energetic Material Detonation Characterization: A Laboratory-Scale Approach. *Propellants, Explos., Pyrotech.* **2013,** *38* (4), 477–485.

List of Symbols, Abbreviations, and Acronyms

AN	ammonium nitrate (NH_4NO_3)
ARL	U.S. Army Research Laboratory
Comp-A5	Composition-A5 (RDX coated with 1.5% stearic acid)
Comp-B	Composition-B (60% RDX, 40% TNT)
CL-20	hexanitrohexaazaisowurtzitane
CN	cyano radical
Epsom salt	magnesium sulfate ($MgSO_4$)
GAP	glyzidyl azide polymer
GNP	graphite nanoparticles
H_2bta	5,5′-bis(1*H*-tetrazolyl)amine
HBT	5,5′-hydrazinebistetrazole
HMX	cyclotetramethylene tetranitramine
HNS	hexanitrostilbene
LIBS	laser-induced breakdown spectroscopy
LSDW	laser-supported detonation wave
m-DNB	1,3-dinitrobenzene
NG	nanographite
p-DNB	1,4-dinitrobenzene
Pentolite	50% TNT, 50% PETN
PETN	pentaerythritol tetranitrate
RDX	cyclotrimethylene trinitramine
TAG-MNT	1-methyl-5-nitriminotetrazolate
TATB	triaminotrinitrobenzene
TMD	theoretical maximum density
TNT	trinitrotoluene

NO. OF COPIES	ORGANIZATION
1 (PDF)	DEFENSE TECHNICAL INFORMATION CTR DTIC OCA
1 (PDF)	DIRECTOR US ARMY RESEARCH LAB IMAL HRA
1 (PDF)	DIRECTOR US ARMY RESEARCH LAB RDRL CIO LL
1 (PDF)	GOVT PRINTG OFC A MALHOTRA
1 (PDF)	US ARMY RSRCH OFC RDRL ROE N R ANTHENIEN
1 (PDF)	US ARMY RSRCH OFC RDRL ROP C J PARKER
2 (PDF)	US ARMY AMRDEC AMSRD AMR PS PT J NEIDERT P JOHNS
1 (PDF)	US ARMY AMRDEC RDMR WPE E M MORRISON
2 (PDF)	RDECOM ARDEC AMSRD AMR SG SD H SAGE S DUNBAR
1 (PDF)	US ARMY ARDEC AMSRD AAR AEE W R DAMAVARAPU
1 (PDF)	US ARMY AMRDEC RDMR WPE E G DRAKE
1 (PDF)	US ARMY TACOM ARDEC AMSRD AAR AEE W E BAKER
2 (PDF)	RDECOM ARDEC RDAR MEM C D DEMELLA P MAGNOTTI
5 (PDF)	US ARMY ARDEC RDAR MEE W E CARAVACA J LAQUIDARA E ROZUMOV J O'REILLY W BALAS-HUMMERS
7 (PDF)	US ARMY ARDEC RDAR MEE W S NICOLICH A DANIELS A DI STASIO M MEZGER K LEE V GOLD S SINGH
1 (PDF)	US ARMY ARDEC RDAR MEE W P ANDERSON
6 (PDF)	US ARMY ARDEC RDAR MEF E D CARLUCCI M HOLLIS C STOUT A SANCHEZ R HOOKE J MURNANE
8 (PDF)	RDECOM ARDEC RDAR MEF S D PANHORST G MINER N GRAY R FULLERTON B DEFRANCO M MARSH P FERLAZZO D PASCUA
3 (PDF)	RDECOM ARDEC RDAR MEM C D NGUYEN D CIMORELLI K SANTANGELO
2 (PDF)	RDECOM TACOM ARDEC RDAR MEM M C MOEHRINGER J TRAVAILLE

NO. OF COPIES	ORGANIZATION
4 (PDF)	RDAR MEM A E VAZQUEZ S CHUNG G MALEJKO W KOENIG
1 (PDF)	RDECOM ARDEC W TOLEDO
3 (PDF)	RDECOM TACOM ARDEC RDAR MEF I R GRANITZKI J CHOI L VO
1 (PDF)	RDECOM ARDEC RDAR MEM C M LUCIANO
1 (PDF)	US ARMY ARDEC RDAR MEE W J LONGCORE
1 (PDF)	RDECOM ARDEC RDAR MEF M HOHIL
1 (PDF)	US ARMY TACOM ARDEC RDAR MEF E T RECCHIA
2 (PDF)	US ARMY TACOM ARDEC SFAE AMO CAS R KIEBLER P MANZ
1 (PDF)	US ARMY ARDEC SFAE AMO CAS EX M BURKE
2 (PDF)	US ARMY ARDEC SFAE AMO CAS MS P BURKE G SCHWARTZ
1 (PDF)	US ARMY TACOM ARDEC SFAE AMO MAS C GRASSANO
1 (PDF)	US ARMY ARDEC SFAE AMO MAS LC D RIGOGLIOSO
1 (PDF)	RDECOM ARDEC RDAR MEM A J GRAU
1 (PDF)	US ARMY PEO AMMO V MATRISCIANO
1 (PDF)	PM MAS SFAE AMO MAS SETI J FOULTZ
1 (PDF)	OFC OF NAVAL RSRCH C BEDFORD
1 (PDF)	OFC OF NAVAL RSRCH ONR 30 D SIMONS
1 (PDF)	NSWC -IHD CODE R13HH H HAYDEN
1 (PDF)	NSWC IHD WARHEADS BRANCH T HENNESSEY
1 (PDF)	NSWC DD P CONOLLY
1 (PDF)	AFRL RWME C LINDSAY
1 (PDF)	US SOC J MORGAN
1 (PDF)	DARPA/DSO J GOLDWASSER
1 (PDF)	DTRA B WILSON
1 (CD)	DIR BENET WEAPONS LAB TECH LIB 1 BUFFINGTON ST WATERVLIET NY 12189-4000
1 (CD)	NAVAL RSRCH LAB TECH LIB 4555 OVERLOOK AVE WASHINGTON DC 20375-5000

NO. OF COPIES	ORGANIZATION
1 (CD)	FIRES DEPUTY MGR EXP MANEUVER WARFARE OFC OF NAVAL RSRCH ONR 30 875 N RANDOLPH ST RM 1155B ARLINGTON VA 22203
42 (PDF)	DIR USARL RDRL WM P BAKER B FORCH R EHLERS RDRL WMM J ZABINKSI RDRL WML P PEREGINO M ZOLTOSKI RDRL WML A W OBERLE RDRL WML B S BUNTE J CIEZAK-JENKINS T JENKINS F DE LUCIA I BATYREV J BRENNAN E BYRD J GOTTFRIED M HURLEY S IZVEKOV M LEADORE W MATTSON J MORRIS J NEWBERRY R PESCE-RODRIGUEZ S PIRAINO-HAYNES B RICE R SAUSA C TAYLOR N TRIVEDI N S WEINGARTEN N DANG E COLLINS RDRL WML C S AUBERT K MCNESBY E BUKOWSKI C MUNSON RDRL WML D R BEYER A KOTLAR RDRL WML E P WEINACHT

NO. OF COPIES	ORGANIZATION
	RDRL WML F M ILG RDRL WML G J SOUTH RDRL WML H J NEWILL RDRL WMP D LYON RDRL WMP G N ELDREDGE

INTENTIONALLY LEFT BLANK.